Gas flows in the circumgalactic medium around simulated high-redshift galaxies

Peter D. Mitchell, Jérémy Blaizot, Julien Devriendt, Taysun Kimm, Léo Michel-Dansac, Joakim Rosdahl, Adrianne Slyz

Monthly Notices
of the
ROYAL ASTRONOMICAL SOCIETY

MNRAS **474,** 4279–4301 (2018) doi:10.1093/mnras/stx3017
Advance Access publication 2017 November 24

Gas flows in the circumgalactic medium around simulated high-redshift galaxies

Peter D. Mitchell,[1]★ Jérémy Blaizot,[1] Julien Devriendt,[1,2] Taysun Kimm,[3,4] Léo Michel-Dansac,[1] Joakim Rosdahl[1] and Adrianne Slyz[2]

[1]*Univ Lyon, Univ Lyon1, Ens de Lyon, CNRS, Centre de Recherche Astrophysique de Lyon UMR5574, F-69230 Saint-Genis-Laval, France*
[2]*Sub-department of Astrophysics, University of Oxford, Keble Road, Oxford OX1 3RH, UK*
[3]*Kavli Institute for Cosmology and Institute of Astronomy, Madingley Road, Cambridge CB3 0HA, UK*
[4]*Department of Astronomy, Yonsei University, 50 Yonsei-ro, Seodaemun-gu, Seoul 03722, Republic of Korea*

Accepted 2017 November 16. Received 2017 November 16; in original form 2017 July 24

ABSTRACT

We analyse the properties of circumgalactic gas around simulated galaxies in the redshift range $z \geq 3$, utilizing a new sample of cosmological zoom simulations. These simulations are intended to be representative of the observed samples of Lyman α (Lyα) emitters recently obtained with the multi unit spectroscopic explorer (MUSE) instrument (halo masses $\sim 10^{10}$–10^{11} M$_\odot$). We show that supernova feedback has a significant impact on both the inflowing and outflowing circumgalactic medium (CGM) by driving outflows, reducing diffuse inflow rates, and by increasing the neutral fraction of inflowing gas. By temporally stacking simulation outputs, we find that significant net mass exchange occurs between inflowing and outflowing phases: none of the phases are mass-conserving. In particular, we find that the mass in neutral outflowing hydrogen declines exponentially with radius as gas flows outwards from the halo centre. This is likely caused by a combination of both fountain-like cycling processes and gradual photoionization/collisional ionization of outflowing gas. Our simulations do not predict the presence of fast-moving neutral outflows in the CGM. Neutral outflows instead move with modest radial velocities ($\sim$50 km s^{-1}), and the majority of the kinetic energy is associated with tangential rather than radial motion.

Key words: galaxies: evolution – galaxies: formation.

1 INTRODUCTION

With the advent of the multi unit spectroscopic explorer (MUSE) instrument it has recently become possible to detect spatially extended Lyman α (Lyα) emission around individual, faint ($M_{\rm UV} \leq -17$), high-redshift ($3 < z < 6$) galaxies (Wisotzki et al. 2016). This emission extends significantly beyond the rest-frame ultraviolet (UV) stellar emission of these galaxies such that the neutral circumgalactic medium (CGM) is being probed over a significant fraction of the associated dark matter halo virial radii. Complementing existing pencil-beam observations of Lyα in absorption (e.g. Péroux et al. 2007; Cooper et al. 2015; Prochaska et al. 2015), these observations are opening a new window on to the high-redshift CGM around galaxies that were too faint for study in spatially extended emission with previous facilities.

Cosmological simulations are the natural tool to interpret these observations within the context of hierarchical structure formation. Hydrodynamical simulations predict that at this mass scale ($M_{\rm H} \sim 10^{11}$ M$_\odot$) and at these redshifts ($3 < z < 6$), the CGM is highly dynamic. A hot, quasi-hydrostatic halo is not expected to have yet formed and filamentary flows of gas can flow directly down to the central regions of hosting dark matter haloes (e.g. Birnboim & Dekel 2003; Ocvirk, Pichon & Teyssier 2008; Brooks et al. 2009; Kereš et al. 2009). In this regime, boundary conditions are all-important, and therefore idealized simulations with non-cosmological initial conditions are arguably not a suitable tool for interpreting observations. Furthermore, both the spatial and temporal density, temperature and velocity structure of the high-redshift interstellar medium (ISM) and CGM is predicted to be complex (e.g. Ceverino & Klypin 2009; Nelson et al. 2015), ultimately limiting the level of confidence that can be placed in simple, idealized, analytic models, even if they are successful in reproducing observational phenomena (e.g. Verhamme et al. 2008; Dijkstra & Kramer 2012; Gronke & Dijkstra 2016).

Even with cosmological simulations, observations of Lyα emission are particularly challenging to interpret, owing to the resonant nature of the line and the multitude of possible emission

★ E-mail: peter.mitchell@univ-lyon1.fr

mechanisms (e.g. Fardal et al. 2001; Taniguchi et al. 2001; Cantalupo et al. 2014; Dijkstra 2014). To accurately model Ly α transfer using hydrodynamical simulations, it is first necessary to form a realistic ISM, including a cold phase, and with the highest spatial resolution possible (Verhamme et al. 2012). This is prohibitively expensive for large dark matter haloes at low redshift: to resolve the thermal Jeans length across four resolution elements at a density, $n_{\rm H} = 10\,{\rm cm}^{-3}$, and temperature, $T = 100\,{\rm K}$, requires a spatial resolution of 13 pc. At present, this is barely within reach for simulations of Milky Way mass haloes that reach $z = 0$, even using the zoom technique (Hopkins et al. 2014). Furthermore, simulating a realistic cold-phase ISM requires modelling a range of physics that is not typically included in cosmological simulations (for example molecular cooling networks and non-equilibrium thermochemistry, radiative transfer from local sources), all of which act to significantly increase the computational cost of such simulations (e.g. Gnedin, Tassis & Kravtsov 2009; Wise et al. 2014; Hu et al. 2016; Katz et al. 2017; Oppenheimer et al. 2016).

At high redshift ($z \geq 3$), the required resolution to resolve the cold-phase ISM is readily achievable at only modest expense in cosmological zoom simulations, particularly for small haloes ($M_{\rm H} \sim 10^{11}\,{\rm M}_{\odot}$) (e.g. Hopkins et al. 2014; Kimm et al. 2015). It is also computationally feasible to reach the required resolution while including more complex physics (for example radiative transfer or chemical networks) for accurately modelling the multiphase ISM, albeit at greater computational expense (e.g. Kimm & Cen 2014; Katz et al. 2017). Furthermore, for small haloes ($M_{\rm H} \sim 10^{11}$) the role of feedback from active galactic nuclei is thought to subdominant (e.g. Booth & Schaye 2009; Crain et al. 2015; Beckmann et al. 2017; Tremmel et al. 2017), reducing the number of modelling uncertainties. As such, the sensitivity of instruments measuring QSO absorption spectra and spatially extended Ly α emission in this mass/redshift regime offer a unique opportunity to test state-of-the-art modelling of the ISM and CGM in the full cosmological context.

To match observational constraints for the stellar properties of galaxies, early star formation in cosmological simulations must be significantly suppressed by stellar feedback processes (e.g. Hopkins et al. 2014; Agertz & Kravtsov 2015; Wang et al. 2015). Accordingly, successful simulations predict strong mass outflows both through, and out of, haloes (e.g. Anglés-Alcázar et al. 2014; Muratov et al. 2015; Wang et al. 2017). This raises the intriguing possibility that spatially extended Ly α emission may be sensitive to feedback (in addition to the gas accretion processes that have already received significant attention in the literature, e.g. Fardal et al. 2001; Dijkstra & Loeb 2009; Faucher-Giguère et al. 2010; Goerdt et al. 2010; Rosdahl & Blaizot 2012). Evidence that outflows may indeed play a role in non-extended Ly α detections already exists thanks to the prevalence of red wings in Ly α line profiles that are observed to be associated with blueshifted low-ionization metal absorption lines in the spectra of massive Lyman-break galaxies (e.g. Steidel et al. 2010). With extended Ly α detections around individual objects now made possible by MUSE, it is therefore timely to review the impact of outflows (and inflows) on the predicted properties of the neutral CGM.

Here we undertake such a study. First, we introduce a sample of 11 high-resolution (14 pc, dark matter particle mass $m_{\rm DM} = 1.3 \times 10^4\,{\rm M}_{\odot}$, stellar particle mass $m_{\star}^{i} = 9.2 \times 10^3\,{\rm M}_{\odot}$) cosmological zoom simulations, specifically designed to interface with the recent progress in high-redshift CGM observations around faint galaxies. We test these simulations against observational constraints on the stellar properties of high-redshift galaxies. The main part of our analysis is then dedicated to quantifying the predicted properties of circumgalactic gas flows and assessing the impact of SN feedback. We place an emphasis on the properties of neutral circumgalactic hydrogen, relevant to both Ly α emission and Lyman-limit systems. Our intention is that the work presented here will serve as a reference point for future work involving processing these simulations with Ly α radiative transfer to enable a detailed comparison with recent observations.

Analyses similar to this study have been undertaken by a number of authors, albeit mostly in different mass/redshift ranges, or at significantly lower resolution. For example, van de Voort et al. (2011) analysed inflow rates in cosmological simulations of a 34 Mpc box at moderate resolution ($m_{\rm gas} = 1.85 \times 10^6\,{\rm M}_{\odot}$), finding that (kinetic) SN feedback does not affect accretion rates on to $10^{11}\,{\rm M}_{\odot}$ haloes at $z = 3$. van de Voort et al. (2012) analysed the same simulations, finding the majority of the neutral CGM at $z = 3$ is inflowing as opposed to outflowing. Faucher-Giguère, Kereš & Ma (2011) analysed inflow rates in cosmological simulations of a 40 Mpc box at slightly lower resolution, finding that hydrodynamically decoupled winds can suppress both the net and inflowing accretion rates of cool gas in $10^{11}\,{\rm M}_{\odot}$ haloes at $z = 3$, but only if very high SN kinetic energy is injected. Nelson et al. (2015) analysed both inflowing and net accretion rates with a 29 Mpc box at similar resolution to van de Voort et al. (2011), using the calibrated subgrid models presented in Vogelsberger et al. (2013), which yield moderate agreement with the observed stellar mass function (Vogelsberger et al. 2014). They found that accretion rates of gas being accreted for the first time on to galaxies hosted by $10^{11.3}\,{\rm M}_{\odot}$ are reduced by a factor $\sim$2 at all redshifts when feedback is included.

Anglés-Alcázar et al. (2014) analysed a suite of 200 pc resolution (maximum) zoom simulations with hydrodynamically decoupled, kinetic supernova-driven winds. They found that the baryon fractions within $10^{11}\,{\rm M}_{\odot}$ haloes at $z = 2$ are reduced to roughly half the cosmological value because of SN feedback. Brook et al. (2014) analysed the baryon cycling within a suite of zoom simulations with thermal supernova feedback (with delayed cooling) and additional thermal energy injection to model the effect of pre-SN processes associated with massive stars. They report mass-loading factors[1] of $\sim$2–3 for haloes of mass, $8 \times 10^{11}\,{\rm M}_{\odot}$, at $z = 0$ (which will evolve, on average, from $\sim 10^{11}\,{\rm M}_{\odot}$ haloes at $z = 3$), simulated with a gas particle mass $2 \times 10^5\,{\rm M}_{\odot}$. Christensen et al. (2016) analysed a suite of zoom simulations also featuring thermal supernova feedback with delayed cooling. They also report similar mass-loading factors (although in this case expressed as the ratio of time-integrated outflow to integrated star formation) for similar mass haloes. Keller, Wadsley & Couchman (2016) analysed a suite of zoom simulations with gas particle mass $m_{\rm gas} = 2.2 \times 10^5\,{\rm M}_{\odot}$. They show that a superbubble model for SN feedback featuring a subgrid multiphase description of outflows can also generate large mass-loading factors ($\eta \sim 8$) in $10^{11}\,{\rm M}_{\odot}$ haloes. Muratov et al. (2015, see also Anglés-Alcázar et al. 2017) performed a comprehensive analysis of outflows from very high resolution zoom simulations featuring thermal and momentum injection from massive stars and SN, and which have been shown to provide a good match to stellar constraints (Hopkins et al. 2014). They also report large mass-loading factors ($\eta \sim 10$) for $10^{11}\,{\rm M}_{\odot}$ haloes at $z = 3$, simulated with gas particle mass, $m_{\rm g} = 5 \times 10^3$–$4 \times 10^4$.

Powell, Slyz & Devriendt (2011) analysed a zoom simulation similar to the simulations presented here, but at higher resolution

[1] Ratio of the mass ejection rate (by feedback) to the star formation rate.

Table 1. Basic properties of our sample of 11 haloes at $z = 3$, each of which is simulated once with SN feedback and once without SN feedback. Properties include halo mass, $M_{\rm H}$, stellar mass, $M_\star$, the number of dark matter particles with the virial radius, $N_{\rm DM}$, and the number of leaf gas cells within the virial radius, $N_{\rm leaf}$.

Halo	$M_{\rm H}$ [Feedback] ($\rm M_\odot$)	$M_\star$ [Feedback] ($\rm M_\odot$)	$M_\star$ [No feedback] ($\rm M_\odot$)	$N_{\rm DM}$ [Feedback]	$N_{\rm leaf}$ [Feedback]
1	6.1×10^9	4.1×10^6	5.0×10^8	4.6×10^5	6.0×10^5
2	9.8×10^9	2.6×10^7	8.3×10^8	7.3×10^5	8.8×10^5
3	1.1×10^{10}	9.4×10^7	1.2×10^9	8.4×10^5	1.1×10^6
4	1.5×10^{10}	3.6×10^7	6.9×10^8	1.1×10^6	1.5×10^6
5	3.2×10^{10}	9.1×10^8	2.3×10^9	2.2×10^6	3.3×10^6
6	3.7×10^{10}	3.1×10^8	3.9×10^9	2.6×10^6	3.8×10^6
7	4.1×10^{10}	1.9×10^8	2.1×10^9	2.9×10^6	4.3×10^6
8	4.2×10^{10}	2.1×10^8	2.4×10^9	3.0×10^6	4.2×10^6
9	4.6×10^{10}	1.8×10^9	1.9×10^9	3.1×10^6	4.3×10^6
10	6.7×10^{10}	7.0×10^8	6.1×10^9	4.8×10^6	7.7×10^6
11	1.1×10^{11}	1.6×10^9	5.8×10^9	8.2×10^6	1.2×10^7

(∼1 pc) and stopping at very high redshift ($z = 9$). They found that cold, filamentary accretion rates are roughly unaffected by SN feedback. Kimm et al. (2015) analysed a suite of zoom simulations (12 pc resolution) of a single halo, very comparable to the more massive haloes presented here (but with lower mass resolution), in this case exploring a range of different SN feedback models. Their mechanical feedback model is the model used in this study. They used an older model for star formation, with a low star formation efficiency and a simple gas density threshold. They report a mass-loading factor (for the mechanical feedback model) ranging from ∼10 at high redshift to ∼0.5 at $z = 3$.

The layout of this paper is as follows. We outline the technical details of our simulations, subgrid models and post-processing analysis methodology in Section 2. In Section 3, we compare our simulations to constraints on the stellar properties of high-redshift galaxies inferred from observations. We illustrate the basic relationship between star formation and gas flows for individual cases in Section 4. We explore the integrated baryon content of our haloes, as well as inflow/outflow rates in Section 5. We explore the properties of diffuse, circumgalactic gas flows in Section 6. We discuss the wider implications and limitations of our results in Section 7 and summarize our results in Section 8.

2 METHODS

2.1 Simulations

The simulations presented in this paper were performed with RAMSES, an Eulerian hydrodynamics code with adaptive mesh refinement (Teyssier 2002). We assume a Λ cold dark matter model with cosmological parameters, $\Omega_{\rm M} = 0.3175$, $\Omega_\lambda = 0.6825$, $\Omega_{\rm B} = 0.049$, $H_0 = 67.11\,{\rm km\,s^{-1}\,Mpc^{-1}}$, $n_{\rm s} = 0.962$ and $\sigma_8 = 0.83$ (Planck Collaboration XVI 2014). The initial conditions were generated with MUSIC (Hahn & Abel 2011). We first run a parent dark matter only simulation of a cosmological box to $z = 3$ with 256^3 particles over a $(20\,{\rm Mpc}\,h^{-1})^3$ volume. Candidate haloes are then identified and Lagrangian regions (corresponding to 150 pkpc radius spheres around these haloes at $z = 3$) are resimulated at high resolution as a series of dark matter only zoom simulations (where the high-resolution region is embedded within the lower resolution cosmological box using the zoom technique). The volumes of the high-resolution regions are set to $(150\,{\rm pkpc})^3$ at $z = 3$. The high-resolution regions are checked for contamination from coarse dark matter particles. Finally, we simulate 11 contaminant-free haloes with full hydrodynamics with halo masses ranging from 10^{10} to $10^{11}\,\rm M_\odot$ at $z = 3$ (again checking for contamination). We simulate each halo both with and without supernova feedback. Basic information about each simulated halo is summarized in Table 1.

The Euler equations are solved using a second-order Gudunov scheme. We use the HLLC Riemann solver, with a MinMod total variation diminishing scheme to reconstruct the intercell fluxes. We use a Courant factor of 0.8. In all of the simulations presented here, we adopt the quasi-Lagrangian refinement criteria that cells are refined inside the zoom region if $\rho_{\rm DM}\Delta x^3 + \frac{\Omega_{\rm DM}}{\Omega_{\rm B}}\rho_{\rm gas}\Delta x^3 + \frac{\Omega_{\rm DM}}{\Omega_{\rm B}}\rho_\star\Delta x^3 > 8m_{\rm DM}^{\rm HR}$, where $\rho_{\rm DM}$, $\rho_{\rm gas}$ and $\rho_\star$ are the respective densities of dark matter, gas and stars, Δx is the cell size and $m_{\rm DM}^{\rm HR}$ is the higher resolution dark matter particle mass. We choose not to include additional refinement criteria based on the thermal Jeans length.[2]

The dark matter particle mass in the zoom region is $1.3 \times 10^4\,\rm M_\odot$. Star particles are formed with a minimum mass of $921\,\rm M_\odot$. By $z = 3$, we allow up to 7 levels of refinement beyond the initial refinement level of the zoom region (12 levels of refinement), corresponding to a leaf cell size of 14 pc (proper) for the highest refinement level at $z = 3$.[3] Note that the resolution in cosmological simulations is highly adaptive, such that 14 pc resolution is only reached inside the ISM. For comparison, the typical resolution in the CGM is typically of the order of ∼100pc (mass-weighted average) or ∼500pc (volume-weighted average).

2.2 Radiative heating/cooling

Gas heating, cooling and (H, He) ionization balance are solved assuming ionization equilibrium for a monoatomic gas with a ratio of specific heat, $\gamma = 5/3$. Photoionization and photoheating from a uniform UV background (Haardt & Madau 1996) is activated after

[2] We have tested the impact of including an additional refinement criterion that ensures that the thermal Jeans length is always resolved over four leaf cells up until the maximum refinement level of the simulation. We find this makes zero qualitative difference to the resulting galaxy/CGM, with quantitative differences at the percent level in galaxy stellar mass and neutral hydrogen mass in the CGM.

[3] From the dark matter only zoom simulations, we find that dark matter alone will lead to a maximum refinement level, $l = 19$, at $z = 3$ with this scheme. In order to reach $l = 21$ for the gas without the AMR grid oversampling DM particles, we compute the density of DM (used for computing the gravitational potential) only down to $l = 19$ (by setting cic_levelmax = 19).

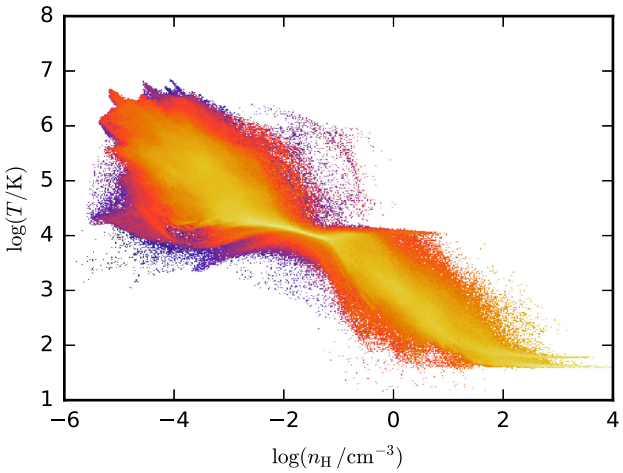

Figure 1. Phase diagram of the gas within the virial radius of an $M_{\rm H} = 10^{10.5}\,{\rm M}_{\odot}$ halo at $z = 3$, simulated with supernova feedback. Gas considered gravitationally bound to satellites has been removed. The colour scheme is scaled logarithmically with the gas mass enclosed in each pixel, ranging from blue at low enclosed mass to yellow-white at high enclosed mass.

redshift, $z = 8.5$. The UV radiation field is exponentially damped in gas cells above the self-shielding density, $n_{\rm H} > 0.01\,{\rm cm}^{-3}$. Metal-line radiative cooling is implemented using tabulated cooling rates from CLOUDY (Ferland et al. 1998) for $T > 10^4$ K. Below $T = 10^4$ K, metal-line cooling is implemented following Rosen & Bregman (1995). In practice, this allows dense ISM gas to cool down to 10 K. We do not include molecular cooling channels and as such the cold-phase ISM that forms in our simulations is at best an approximation of a realistic cold phase. Gas in the initial conditions is assigned a metallicity of $Z = 10^{-4}\,{\rm Z}_{\odot}$ to help mimic the effects of molecular line cooling in unresolved low-mass mini-haloes at high redshift. In practice, this acts to increase the amount of star formation that can occur in low-mass satellites of our target haloes.

A typical T–ρ diagram for a simulation with supernova feedback is shown in Fig. 1 for an $M_{\rm H} = 10^{10.5}\,{\rm M}_{\odot}$ halo at $z = 3$. We do not artificially pressurize gas that otherwise cools below a polytrope $P(\rho)$. This means that a plausibly realistic ISM density distribution can form, which is a requirement for performing realistic Ly α radiative transfer through the ISM.

2.3 Star formation and chemical enrichment

We utilize the thermo-turbulent subgrid scheme for star formation first introduced in Kimm et al. (2017) and fully described in Devriendt et al. (in preparation). In this scheme, both thermal and turbulent pressure support terms are balanced against gravity to determine the threshold for stability against collapse. Gas cells that are deemed unstable then form stars following a Schmidt law, with an efficiency per freefall time that is scaled to the local ISM conditions, following Federrath & Klessen (2012).

The star formation threshold relies on the computation of a thermo-turbulent Jeans length, $\lambda_{\rm J,\,turb}$ (Federrath & Klessen 2012), which accounts for both thermal and non-thermal pressure support,

$$\lambda_{\rm J,turb} = \frac{\pi\sigma_{\rm gas}^2 + \sqrt{36\pi c_{\rm s}^2\, G\Delta x^2 \rho_{\rm gas} + \pi^2\sigma_{\rm gas}^4}}{6\, G\rho_{\rm gas}\Delta x} \tag{1}$$

where $\sigma_{\rm gas}$ is the gas velocity dispersion measured on some physical scale, Δx, $\rho_{\rm gas}$ is the gas density and $c_{\rm s}$ is the sound speed. For the implementation here, Δx is the cell size and $\sigma_{\rm gas}$ is computed from a first-order Taylor expansion of the velocity field around the centre of a given gas cell (Devriendt et al., in preparation). Gas cells are considered to be unstable if $\lambda_{\rm J,\,turb} \leq \Delta x$.

For cells deemed to be unstable, star formation is implemented as a Schmidt law,

$$\frac{{\rm d}\rho_{\star}}{{\rm d}t} = \epsilon_{\rm ff}\frac{\rho_{\rm gas}}{t_{\rm ff}}, \tag{2}$$

where $\rho_{\rm gas}$ is the gas density and $t_{\rm ff} = \sqrt{3\pi/32G\rho_{\rm gas}}$ is the characteristic freefall time-scale (Schmidt 1959). Stellar particles are formed using equation (2) as a Poissonian process.

Contrary to a standard implementation used in cosmological simulations, the efficiency factor, $\epsilon_{\rm ff}$ is not set to a constant, low value above some density threshold, consistent with observations of star formation over ∼kpc scales. Instead, the 14 pc resolution of the ISM in our simulations motivates the use of an efficiency per freefall time that scales with the local ISM conditions. In this case, the local star formation efficiency per freefall time can be significantly higher than the ∼1 per cent efficiencies implied by observations over kpc scales (up to and beyond ∼100 per cent efficiency).

$\epsilon_{\rm ff}$ is computed by first assuming that within a given gas cell, there is an unresolved density distribution function of lognormal form, and that there is a critical density in this distribution above which gas can collapse to form stars. From this distribution, a density-weighted integral of the freefall efficiency ($t_{\rm ff}^{-1}(\rho)$) is performed for all densities, ρ, above the threshold, expressed here as the density contrast, $\sigma_{\rm crit}$. $\epsilon_{\rm ff}$ is then given by normalizing this integral with the corresponding freefall efficiency evaluated at the average density of the gas cell, ρ_0. Put together, this is written as

$$\epsilon_{\rm ff} = \frac{\epsilon_{\rm acc}}{2\phi_{\rm t}}\exp(3\sigma_{\rm s}^2/8)\left[1 + {\rm erf}\left(\frac{\sigma_{\rm s}^2 - s_{\rm crit}}{\sqrt{2\sigma_{\rm s}^2}}\right)\right], \tag{3}$$

where $\sigma_{\rm s}^2$ is the standard-deviation width of the lognormal probability distribution function, expressed in terms of the logarithmic, dimensionless density contrast, $s \equiv \ln(\rho/\rho_0)$. $\epsilon_{\rm acc}$ and $\phi_{\rm t}$ are dimensionless model parameters. $\epsilon_{\rm acc}$ accounts for the mass that is returned to the ISM from protostellar objects by jets and outflows and is set to 0.5, following empirical constraints (see Federrath & Klessen 2012). $\phi_{\rm t}$ accounts for the uncertainty associated with the idealized calculation for freefall time-scale of molecular clouds and is set to 0.57, which is the best-fitting value from the numerical simulations of Federrath & Klessen (2012). Assuming the lognormal probability density distribution function is a physical consequence of isothermal, supersonic turbulence, the distribution width is given by $\sigma_{\rm s}^2 = \ln(1 + b^2\mathcal{M}^2)$ (Federrath & Klessen 2012). Here, b (set to 0.4) characterizes the balance of solenoidal and compressive modes for driving turbulence and $\mathcal{M} \equiv \sigma_{\rm gas}/c_{\rm s}$ is the sonic Mach number.

The critical logarithmic overdensity threshold for local collapse, $\sigma_{\rm crit}$, is computed using the model of Padoan & Nordlund (2011),

$$s_{\rm crit} = \ln(0.067\theta^{-2}\alpha_{\rm vir}\mathcal{M}^2), \tag{4}$$

where θ is a numerical parameter calibrated to reproduce results from the numerical simulations of Federrath & Klessen (2012). $\alpha_{\rm vir} \equiv 2E_{\rm k}/|E_{\rm grav}|$ is the virial parameter, approximated here as

$$\alpha_{\rm vir} = \frac{5(\sigma_{\rm gas}^2 + c_{\rm s}^2)}{\pi\rho_{\rm gas}G\Delta x^2}, \tag{5}$$

where (as in equation 1) $\rho_{\rm gas}$ is the gas density in the cell, $\sigma_{\rm gas}$ is the gas velocity dispersion and Δx is the cell size.

2.4 Supernova feedback

We include momentum and thermal energy injection from Type II supernovae as the sole source of feedback in our simulations. The scheme for supernova feedback was introduced in Kimm & Cen (2014, see also Hopkins et al. 2014, 2017), has been described subsequently in Kimm et al. (2015) and Kimm et al. (2017), and has been compared to other common supernova feedback schemes in Rosdahl et al. (2017) for high-resolution, idealized disc simulations. Here, we adopt prior convention by referring to this scheme as 'mechanical feedback'. We do not use the extensions to this scheme introduced in (Kimm et al. 2017, pre-processing of the ambient ISM by photo-ionizing photons, Geen et al. 2015) or (Kimm et al. 2015, temporally spaced supernova explosions and modelling porosity effects on unresolved scales).

The rationale for the mechanical feedback scheme is similar to that of the thermo-turbulent star formation model. Namely, that when the ISM is both resolved significantly below kpc scales and a cold phase is allowed to form, it is desirable to use a feedback scheme designed to exploit both the high spatial resolution and that the local ISM conditions around supernova explosions are plausibly realistic.[4] Specifically, at high enough resolution simulations can resolve the distinct stages of Sedov–Taylor SN explosions. If the surrounding ISM conditions are also realistic, the associated subsequent radiative losses that occur on resolved scales should be accurately captured. With knowledge of which stage of the SN explosion is spatially resolved (at the time of energy/momentum injection), the radiative losses and kinetic/thermal energy exchanges that occur on unresolved scales can then be modelled 'subgrid' in a physically self-consistent manner.

In the mechanical feedback scheme, momentum and thermal energy are injected into neighbouring cells around the host cell of a given supernova explosion. SN explosions are assumed to occur 10 Myr after the formation of a given stellar particle. For each neighbouring cell, a local calculation is performed to determine if the explosion is resolved in the energy conserving Sedov–Taylor stage or the momentum conserving snowplow phase (see Kimm & Cen 2014; Kimm et al. 2015, for details). For the former, Δp of radial momentum is injected as

$$\Delta p = f_{\rm c}\sqrt{2\chi(\Omega) m_{\rm ej} f_{\rm e} N_{\rm SN} E_{\rm SN}}, \quad (6)$$

where $N_{\rm SN}$ is the number of supernova explosions that occur inside a given host cell, $E_{\rm SN} = 10^{51}$ erg is the canonical energy of individual supernova explosions, $f_{\rm c}$ is the fraction of the total outflowing mass in the neighbouring cell, $m_{\rm ej}$ is the initial mass of the SN ejecta, $f_{\rm e}$ is a factor which ensures a smooth transition between the adiabatic and snowplow phases and $\chi(\Omega)$ is the local mass-loading factor (see Kimm & Cen 2014; Kimm et al. 2015, for details).

For the case of neighbouring cells where the explosion is initially resolved in the snowplow phase, momentum is instead injected as

$$\Delta p = 3\times10^5\,{\rm km\,s^{-1}}\, f_{\rm c} E_{51}^{16/17} n_0^{-(2/17)} Z'^{-0.14}, \quad (7)$$

where E_{51} is the initial supernova energy ($N_{\rm SN}E_{\rm SN}$) in units of 10^{51} erg, n_0 is the local ambient ISM hydrogen number density in units of $1{\rm cm}^{-3}$, and $Z' = \max(Z/{\rm Z}_\odot, 0.01)$ is the local ISM metallicity.[5] If the momentum injection into a given cell reduces the net kinetic energy (injected kinetic energy plus pre-existing kinetic energy) because of vector cancelling of velocities, thermal energy is injected to make up the difference.

We choose model parameters such that the SN energy injected per unit stellar mass formed is $2\times10^{16}\,{\rm erg\,g^{-1}}$. With a Chabrier (2003) stellar initial mass function (truncated below $0.1\,{\rm M}_\odot$ and above $100\,{\rm M}_\odot$), and taking the minimum SN progenitor mass to be $8\,{\rm M}_\odot$, the energy from SN injected per unit stellar mass formed is $5.94\times10^{15}\,{\rm erg\,g^{-1}}$ (assuming individual SN contribute 10^{51} erg). In practice, we find that our simulations significantly overpredict the stellar masses of galaxies with respect to extrapolations of observational constraints if we adopt this value. To improve this situation, we have pragmatically opted to increase the energy injected by SNe up to $2.0\times10^{16}\,{\rm erg\,g^{-1}}$, which represents an increase by a factor 3.4.

There are a number of possible justifications for this energy enhancement. First, if we instead take the minimum SNe progenitor mass as $6\,{\rm M}_\odot$, our adopted parameters represent a factor 2.3 over-injection of energy (this follows from stellar models with convective overshoot which predict that 6–8 $\rm M_\odot$ stars explode as electron capture SNe; Chiosi, Bertelli & Bressan 1992). Secondly, our model for feedback from massive stars only includes energy from supernova explosions, neglecting possible contributions from, for example, stellar winds, radiation and cosmic rays. Increasing the SNe energy by a factor 2 to account for this, if not an accurate way to take these processes (as we do not pre-process the ISM before SN explode), is certainly energetically feasible (e.g. Agertz & Kravtsov 2015). We discuss these issues further in Section 7.3.

As well as injecting energy and momentum into the neighbouring gas cells, star particles also release 20 per cent of their mass (so $m_{\rm ej} = 0.2m_\star^i$, where $m_\star^i$ is the initial stellar particle mass) and inject metals with a yield of 0.05 (as for the SN explosions, this occurs 10 Myr after the stellar particle formation time). Stellar mass loss and metal enrichment from stellar evolution therefore only occurs for our simulations which include SN feedback.

2.5 Halo identification and tree construction

Haloes are identified from the dark matter particle distribution using the AdaptaHOP algorithm (Aubert, Pichon & Colombi 2004), and merger trees are constructed following Tweed et al. (2009). In practice, the only information from the halo finder which is used in this study is the central positions of subhaloes (which are taken to be the position of the density maxima) and the distinction in hierarchy between central and satellite subhaloes. We measure halo masses and virial radii by computing the spherical radius within which the mean enclosed density is 200 times the critical density of the Universe at a given epoch.

2.6 Baryon compartmentalization

To analyse the CGM content of our simulated haloes, we split the baryons enclosed within the virial radius of a given halo into a number of components. First, we divide hydrogen between neutral and ionized phases, using the internal RAMSES calculation described in Section 2.2. We further subdivide ionized hydrogen at a temperature, $T = 10^{4.5}$ K, into warm-ionized and hot-ionized phases. This acts to approximately separate between photoionized hydrogen at $T\sim10^4$ K and collisionally ionized hydrogen at hotter temperatures (see the phase diagram in Fig. 1). We also split each gas phase into radially inflowing and outflowing components.

The relationship between these various gas phases is illustrated in Fig. 2, which shows a series of projected density maps for the

[4] By this we mean simply that we have not artificially pressurized dense gas below a certain temperature.

[5] We use a solar metal mass fraction of $Z_\odot = 0.02$ throughout.

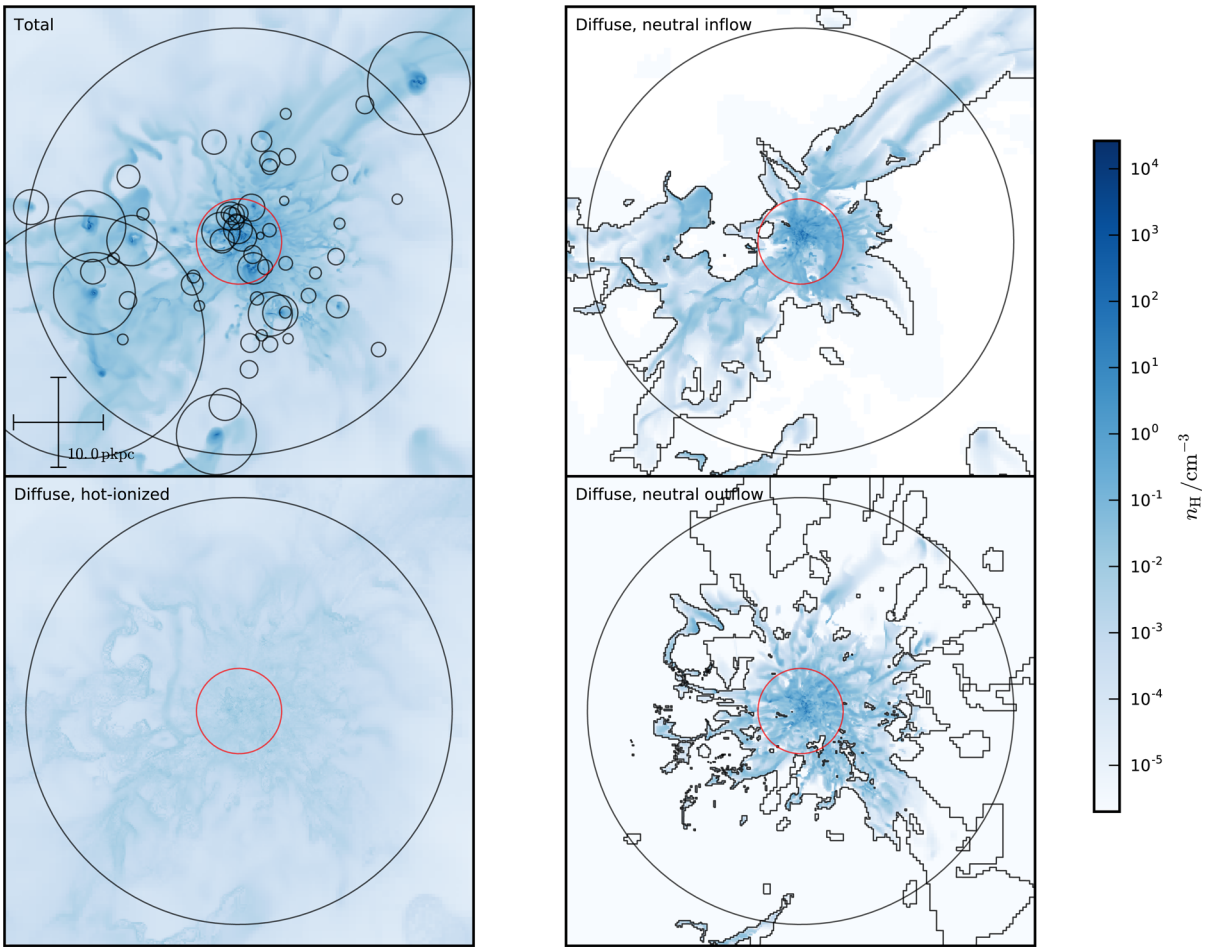

Figure 2. The CGM around an $M_H = 10^{11}$ M$_\odot$ halo at $z = 3.9$, simulated with supernova feedback (halo 11 in Table 1). Each panel shows a density map for a different gas selection. Density maps are computed as a density-weighted average gas density along the line of sight in each pixel. The density map in the top-left panel includes all gas within a cube around 1.1 of the virial radius. Other panels show diffuse gas (meaning gas considered gravitationally bound to satellites is removed). These include the hot-ionized phase (bottom-left), neutral inflow (top-right) and neutral outflow (bottom-right). For the right-hand panels, the black contours enclose the warm-ionized phase in inflow (top-right) and outflow (bottom-right). Large black circles indicate the virial radius, R_{vir}. Red circles indicate $0.2R_{vir}$, the radius used to separate the ISM and CGM in parts of our analysis. Small black circles mark the tidal radii of satellites. The black cross has a diameter of 10 kpc (proper).

most massive halo in our sample at $z = 3.5$ (during an outflow event). This halo has a mass, $M_H = 10^{11}$, at $z = 3$. There is a clear visual distinction between the filamentary distributions of neutral and warm-ionized inflow, the distributions of warm-ionized and neutral outflow, and the volume filling distribution of the hot-ionized phase.

A second step in our definition of the CGM is that unless otherwise stated, we exclude gas considered to be gravitationally bound to satellites from our analysis. Specifically, we compute a tidal radius for each satellite subhalo, and subtract baryonic material enclosed within this radius. To approximate the tidal radius, r_t, we follow Binney & Tremaine (2008) and set

$$r_t = R_0 \left(\frac{m}{M(R_0)\left(3 - \frac{\mathrm{d}\ln M}{\mathrm{d}\ln(R)}|_{R=R_0}\right)} \right)^{1/3}, \quad (8)$$

where R_0 is the distance from the satellite centre to the host centre, $M(R_0)$ is the mass of the host enclosed within R_0 and m is the mass of the satellite (the mass within r_t). This relation is appropriate for a satellite on a circular orbit within a spherically symmetric host.

Finally, in Section 5.3, we compare the mass in the CGM with different components of our simulated galaxies. Out of necessity, we introduce a distinction between the central galaxy and the CGM by dividing at $r = 0.2\,R_{vir}$ (indicated by the red circle in Fig. 2). This radius approximately marks the point below which there starts to be a significant amount of mass in $n_H > 1\,\mathrm{cm}^{-3}$ gas, characteristic of the ISM.

2.7 Stellar luminosities

To compare with observations, we predict the luminosities of our galaxies at different wavelengths. To compute luminosities for stellar particles, we use the stellar population synthesis models presented in Bruzual & Charlot (2003). We assume a Chabrier (2003) initial mass function. The Bruzual & Charlot (2003) spectral models are computed for a grid of stellar ages and metallicities. We compute spectra on a particle-by-particle basis by interpolating linearly in age and logarithmically in metallicity. Spectra for each particle are then convolved with the desired filter bandpass to compute luminosities and magnitudes. We do not attempt to account for the attenuation of starlight by dust and we do not include any additional

emission mechanisms (for example, nebula line emission from H II regions) beyond those included in the Bruzual & Charlot (2003) models.

2.8 Gas fluxes

We measure fluxes through spherical surfaces to quantify the flows of gas through the CGM of our simulated galaxies. Fluxes are computed separately for inflowing and outflowing components and unless otherwise stated we remove gas considered bound to satellites from the measurements. To compute the flux of gas at the surface of a sphere, we finely sample the surface with N points[6] and then compute the gas cell which encloses each point. For example, the mass flux of inflowing gas through the surface is then given by

$$\dot{M} = 4\pi R^2 \frac{1}{N} \sum_{i=1}^{N_{\rm inflow}} \rho_{{\rm gas},i}\, v_{{\rm rad},i}, \tag{9}$$

where R is the radius of the surface, $\rho_{{\rm gas},i}$ is the density of the cell enclosing a point, i, on the surface, $v_{{\rm rad},i}$ is the corresponding radial velocity of that cell and $N_{\rm inflow}$ is the number of surface points associated with inflowing cells (that are not enclosed within the tidal radii of satellites).

This approach can be generalized to compute radial profiles of various scalar quantities. Equation (9) represents the specific case of computing $\mathrm{d}p/\mathrm{d}r$, the total radial momentum per unit radius across a spherical surface (which is equivalent to the mass flux, $\mathrm{d}m/\mathrm{d}t$). By removing $v_{{\rm rad},i}$ from the expression, we can compute the radial mass profile, $\mathrm{d}m/\mathrm{d}r$. By replacing $v_{{\rm rad},i}$ with specific energy (either thermal or kinetic) or metallicity, we can compute the radial energy and metallicity profiles, $\mathrm{d}E/\mathrm{d}r$ and $\mathrm{d}Z/\mathrm{d}r$.

3 MODEL VALIDATION

To validate our numerical simulations as a tool for studying the CGM, we first establish the extent to which they provide a reasonable description of faint, high-redshift galaxies. To do so, we compare to constraints inferred from observations for galaxy stellar masses, star formation rates and sizes.

In Fig. 3, the stellar masses of our simulated galaxies are plotted as a function of halo mass. The distribution of points can be compared to the black lines, which show empirical constraints from abundance matching (Behroozi et al. 2013; Moster et al. 2013). This comparison represents the zeroth-order constraint for samples of cosmological zoom simulations, for which it is not possible to predict the stellar mass function. The abundance matching studies shown here are constrained at $z \geq 3$ by observational data sets which are insufficiently deep to probe the stellar mass range shown here ($M_\star < 10^9\,\mathrm{M}_\odot$), and as such the relations shown represent extrapolations (both from higher mass galaxies at $z \leq 4$ and from lower mass galaxies at lower redshift).

When feedback is included (black points), our simulations appear in reasonable agreement with the extrapolated empirical constraints at $z = 3$ for the low-mass haloes in our sample ($\log(M_{\rm H}/\mathrm{M}_\odot) < 10.5$). On the other hand, it appears that the simulated sample has stellar masses that are too slightly high[7] over the halo mass range, $\log(M_{\rm H}/\mathrm{M}_\odot) > 10.5$. Compared to the extrapolated best-fitting abundance matching estimates, our simulated galaxies in this mass range have stellar masses that a factor 7–8 too large on average, although the scatter at fixed halo mass is significant. Compared to the no-feedback case, including SN feedback for these haloes reduces stellar masses by roughly a factor 7 (although notably halo 9 from Table 1 has almost the same stellar mass with and without feedback). Including feedback also reduces halo masses (see Schaller et al. 2015), which is not accounted for in abundance matching and therefore artificially increases the level of disagreement by a small amount.

Given that the abundance matching relations represent extrapolations in this mass range at these redshifts, we choose to also show results from the reference EAGLE simulation (Schaye et al. 2015, blue points). The reference EAGLE simulation is a large volume simulation ($100^3\,\mathrm{Mpc}^3$) which was explicitly calibrated to reproduce the local stellar mass function and has been shown to be consistent with observational constraints on the high-redshift stellar mass function (Furlong et al. 2015). While observational constraints in the relevant mass/redshift range for this study are not available, EAGLE does in effect provide a different way to extrapolate the observed high-redshift stellar mass functions down to lower stellar masses, acting as a consistency check with the abundance matching estimates. EAGLE is indeed consistent with the abundance matching extrapolations in the halo mass range where galaxies are well resolved (at approximately $M_{\rm H} \geq 10^{10}\,\mathrm{M}_\odot$), despite halo masses being reduced by baryonic effects such as feedback (Schaller et al. 2015). We note also that in the mass range shown, the distributions from EAGLE are unaffected by AGN feedback.[8] On balance, the combined picture from EAGLE and abundance matching suggests that it is likely that feedback from stars is too weak in our simulations in the $\log(M_{\rm H}/\mathrm{M}_\odot) > 10.5$ range, although the extrapolation involved means that it is not possible to form a definitive conclusion.

We have also compared our simulations to observational constraints on galaxy star formation rates and galaxy sizes (not shown). From these comparisons, we find no obvious tension with the observational data if we extrapolate the observed trends. As with the stellar masses, the data are insufficiently deep to be truly constraining.

3.1 Detectability and the Ly α–CGM connection

As well as assessing the realism of simulated galaxies, another simple question is whether our simulated galaxies (intended to be representative of the Wisotzki et al. 2016, Ly α-emitter sample) would be detectable in the rest-frame UV in a deep field observed with *Hubble Space Telescope* (*HST*). This question is answered in Fig. 4, which shows that the brighter galaxies that we simulate are indeed comparable in terms of UV luminosities to the Wisotzki et al. (2016) sample. While we also simulate galaxies that are fainter than those detected in Wisotzki et al. (2016), we note that spatially extended Ly α is detected around Ly α emitters that are formally undetected in the rest-frame UV by *HST*. The simulated galaxies that are fainter than this sensitivity limit may therefore still be of interest in future work where we will compare the simulations and

[6] N is set to 10 multiplied by the number of gas cells expected to intersect the surface. The surface points form a regular grid in spherical coordinates and so all surface points have equal solid angle. We find that the fluxes are well converged with respect to increasing N.

[7] Despite the fact that we overinject SN energy by a factor ≈2–3; see Section 2.4.

[8] We have checked this by comparing to an EAGLE simulation run without AGN feedback.

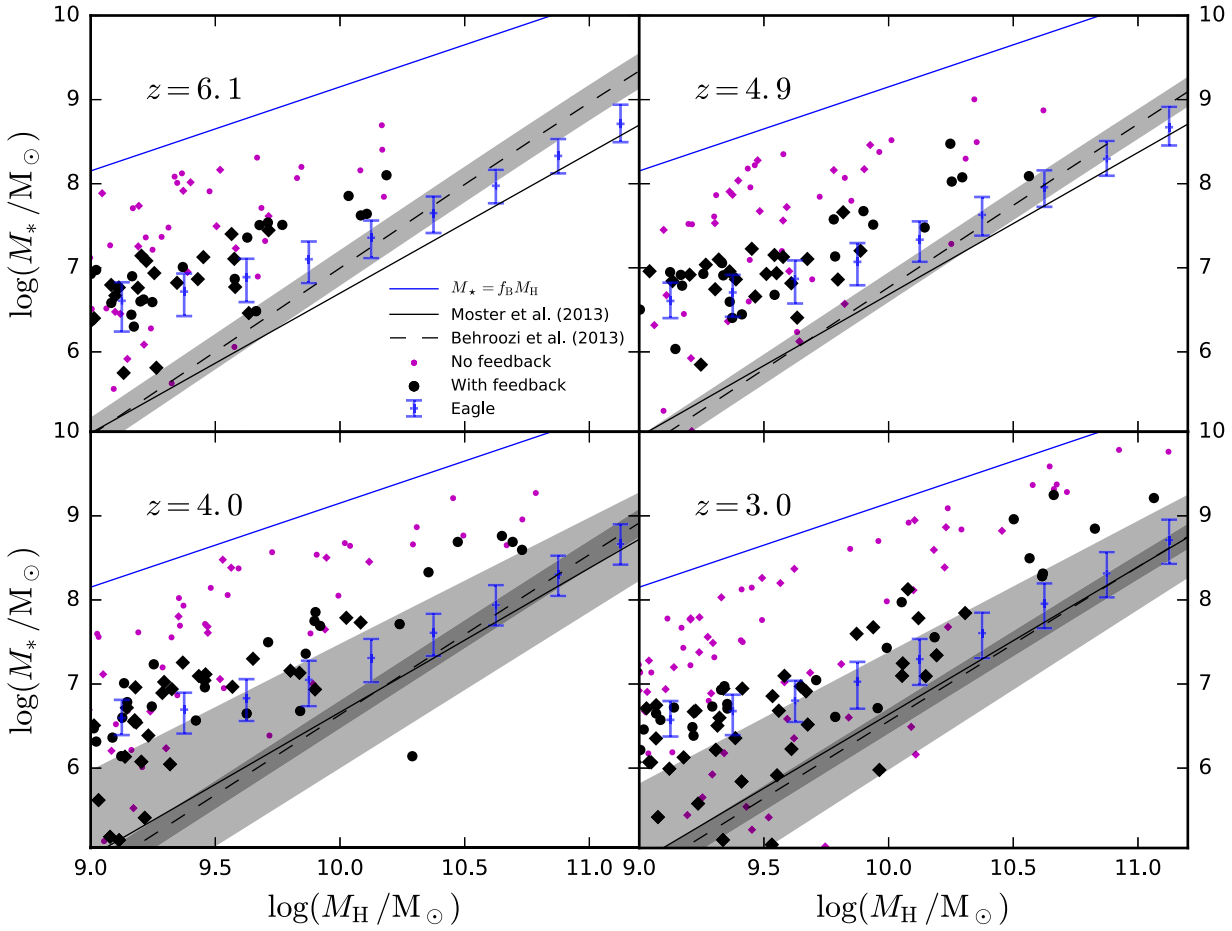

Figure 3. Stellar mass as a function of halo mass for four different redshifts. Small magenta points show galaxies simulated without SN feedback. Large black points show galaxies simulated with SN feedback. Circles indicate central galaxies and diamonds indicate satellites. Stellar masses are computed by summing the stellar mass within 0.2 of the halo virial radius. For satellite galaxies, the halo mass plotted is the maximum past progenitor mass extracted from the merger trees. Blue data points show the 16th, 50th and 84th percentiles of the distribution from the reference EAGLE simulation. The blue line indicates maximal conversion of baryons into stars, assuming the baryon fraction of total mass accreted through the virial radius is equal to the universal value. The black lines (dashed, solid; Behroozi, Wechsler & Conroy 2013; Moster, Naab & White 2013) show extrapolations to empirical constraints from abundance matching modelling. Grey shaded regions show extrapolations to the quoted 1σ uncertainties from these studies (which are only available for $z \leq 4$ for Moster et al. 2013).

observations in terms of spatially extended Ly α emission. We do not attempt to model attenuation of UV photons by dust, and so the UV luminosities of our simulated galaxies will be overestimated, likely by 1 mag or less (Bouwens et al. 2016).

Fig. 4 also demonstrates that the extended Ly α emission observed by Wisotzki et al. (2016) likely traces a significant fraction of the halo virial radius, supporting the interpretation that these observations trace the neutral CGM around high-redshift galaxies (see also Leclercq et al. 2017, for a similar analysis with a larger sample). Incidentally, given that the detected emission is always enclosed within the associated halo virial radii, the choice to truncate our analysis of the CGM at the halo virial radius is reasonable within the context of interpreting extended Ly α emission.

4 FLOWS OF GAS IN SINGLE OBJECTS

Before presenting an analysis of the entire sample, it is illustrative to first consider single objects. The lower mass haloes from our sample are particularly well suited for this purpose because individual episodes of star formation and mass outflows are cleanly separated in time, highlighting the relationship between star formation and outflows.

Fig. 5 shows the star formation history, as well as the inflowing and outflowing fluxes of gas for a halo with a final mass of $\log(M_\mathrm{H}/\mathrm{M}_\odot) = 10.1$ at $z = 3$ (halo 3 in Table 1). The top panel illustrates the temporal relationship between inflow and star formation. Inflowing gas crosses the virial radius (green line) and a comparable mass also crosses an inner surface at 0.25 of the virial radius (solid blue line). Inflow through the inner surface (which can be regarded as the accretion rate of the galaxy) is less steady than the inflow into the halo. From visual inspection, the spikes seen in the inflowing flux through the inner surface are related to galaxy mergers (the corresponding fluxes when material that is gravitationally bound to satellites is included are shown by the dashed blue line).

The star formation history in this halo is very bursty, with individual bursts typically occurring over a duration of ∼50 Myr. Comparing the star formation history with the inflow through $0.25R_\mathrm{vir}$, it is apparent that the vast majority of the inflowing gas is not converted into stars. It is also apparent that some of main bursts of star formation are preceded by a significant positive fluctuation in the

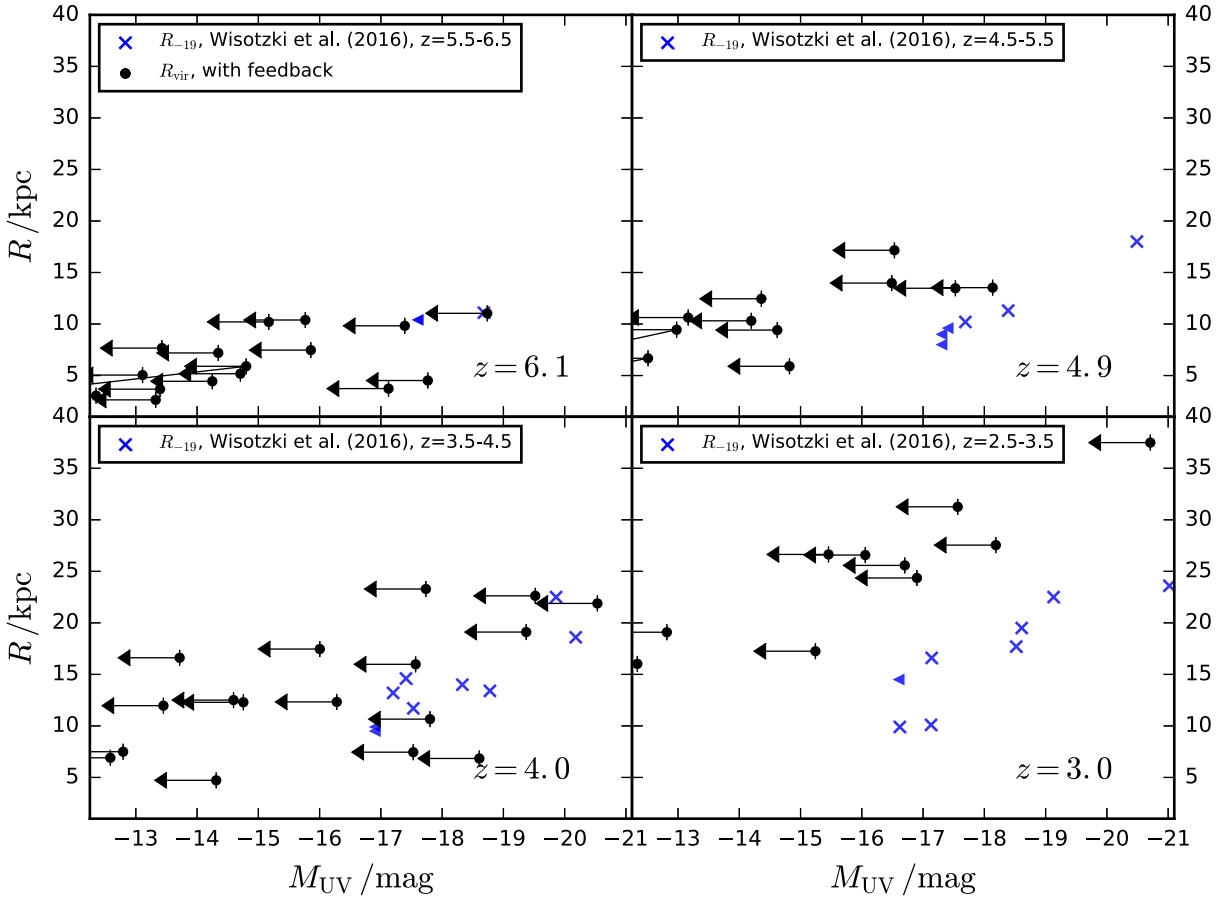

Figure 4. The neutral CGM scales traced by extended Ly α emission. Black points show simulated halo virial radii for central galaxies as a function of rest-frame ∼1500 Å UV absolute magnitude (not including any correction for dust). Halo virial radii are shown to act as a reference point for the physical scales associated with the analysis presented in this study. They are to be compared to isophotal radii, R_{-19}, (blue crosses) that indicate the limiting sensitivity of spatially extended Ly α emission in the Wisotzki et al. (2016) observational sample. From this comparison, we see that Ly α emission traces gas over a significant fraction of the virial radius. Blue triangles indicate upper limits to the UV luminosity for galaxies in the Wisotzki et al. (2016) that are undetected with *HST*. The observed data are not corrected for dust attenuation. To serve as a visual guide, black arrows indicate the typical 1 mag dust attenuation estimated for galaxies at these magnitudes/redshifts (Bouwens et al. 2016). Each panel corresponds to a different redshift, as labelled. Observed Ly α emitters have been binned in redshift accordingly, as labelled. Note that because of sensitivity limits and surface brightness dimming, R_{-19} should not be interpreted as the intrinsic size of Ly α haloes.

inflow rate, but others are not. This serves to underline that there are local processes within the simulated central galaxy besides the gas accretion rate that control the star formation rate.

A different perspective is shown by the second panel of Fig. 5, which compares the star formation history (in units of mass rate) to the gas mass within $0.25R_{\rm vir}$. The twin bursts of star formation that occur just after $z = 5$ are associated with a large increase in the total gas mass. These twin bursts are then followed by a significant reduction in the ISM gas mass. Later bursts also affect the growth of the ISM mass in a similar manner.

The third panel of Fig. 5 illustrates the temporal relationship between star formation and mass outflows. In this panel, we show the star formation taking place within two spherical apertures and the corresponding outflowing mass flux of gas at those radii. There is a clear and simple relationship between star formation episodes and strong mass outflow events. Star formation takes place and (after a small but finite delay) is followed by outflow events characterized by an exponentially decaying temporal profile. The time delay can be partly attributed to our modelling of mechanical Type II SN feedback, where the time delay between stars forming and SN explosions is 10 Myr. From the area under the star formation and outflow fluxes, it is readily apparent that the mass ejected from the galaxy is significantly larger than the mass turned into stars. At $z = 3$, the ratio of time-integrated outflow to star formation is approximately 10. Correspondingly, by comparing to the second panel, it can be inferred that the reduction in gas mass that occurs after star formation bursts is primarily because of outflows, rather than from star formation. The third panel of Fig. 5 also illustrates the role of satellites in driving outflows. The star formation that occurs beyond $0.25\,R_{\rm vir}$ is associated with satellite galaxies (this occurs once just after $z = 6$). This star formation then drives outflows out through the surfaces at 0.5, 1 $R_{\rm vir}$.

The bottom panel of Fig. 5 splits the outflowing mass flux (shown in the third panel) into neutral and ionized phases of hydrogen. This illustrates that the majority of hydrogen mass in the outflow is ionized, but that there is also a residual amount of mass in neutral hydrogen. The importance of neutral outflows does however increase with increasing redshift. Neutral outflow events at a given surface in the halo lag behind ionized outflows, forming a clear temporal sequence.

While the relative simplicity of the simulated halo shown in Fig. 5 makes it ideally suited to illustrate the temporal

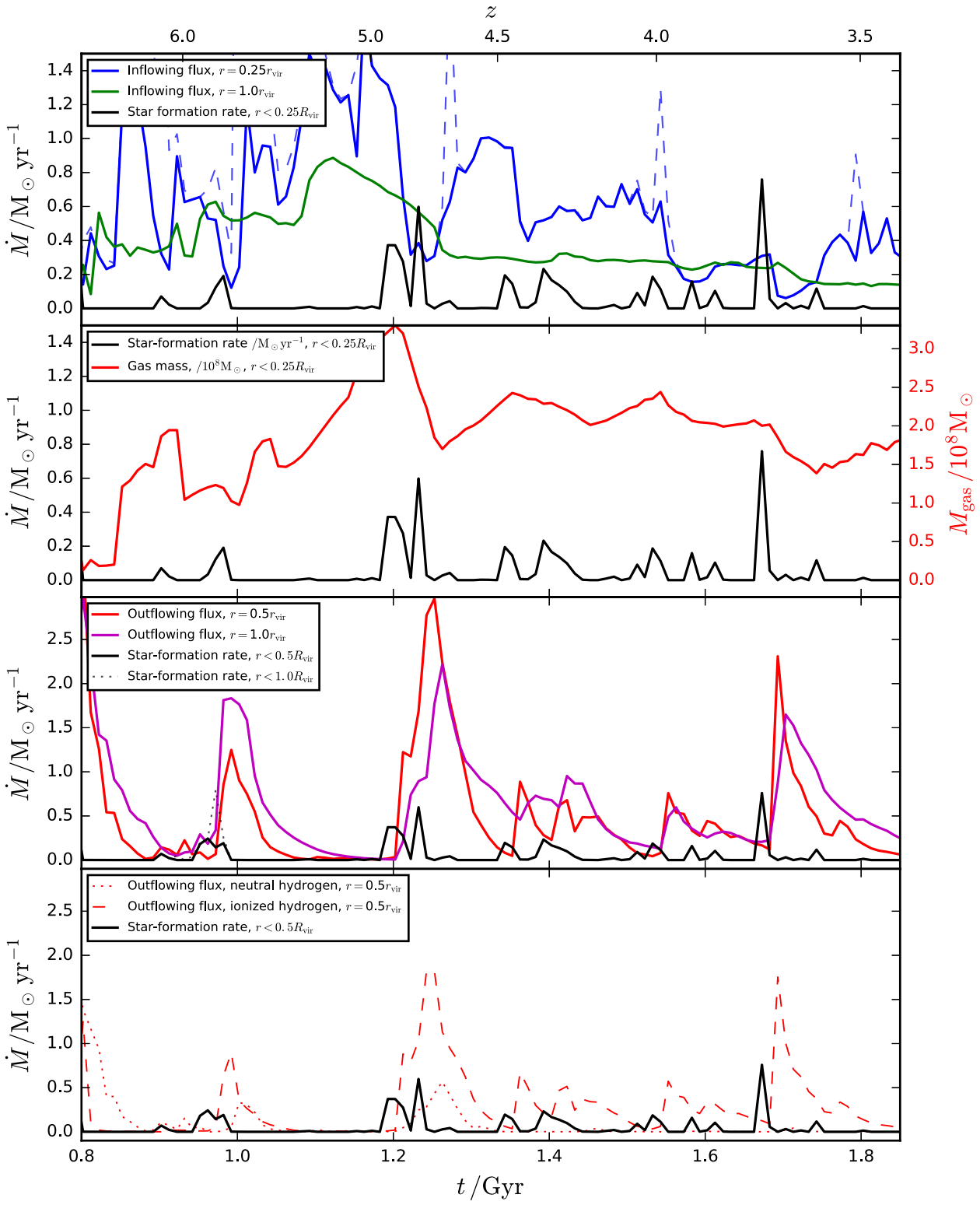

Figure 5. Star formation and flux histories of a simulated halo of mass, $\log(M_{\rm H}/{\rm M}_\odot) = 10.1$ at $z = 3$ (halo 3 in Table 1). *Top:* flux of inflowing gas through the virial radius (green) and through a surface at 0.25 of the virial radius (solid blue). A dashed blue line shows the flux of inflowing gas through the 0.25 surface, in this case including gas that is gravitationally bound to satellites. Also shown is the star formation rate (black) for stars forming within 0.25 of the virial radius. *Second:* star formation rate (black) for stars forming within 0.25 of the virial radius is compared to the total gas mass within the same radius (red). Note that the units of the two lines are different (see left and right axes labels). *Third:* flux of outflowing gas through the virial radius (magenta) and through a surface at 0.5 of the virial radius (red). Also shown is the star formation rate for stars forming within 0.5 of the virial radius (solid black), and within the virial radius (dotted black). *Bottom:* flux of outflowing neutral (dashed red) and ionized (dotted red) hydrogen through a surface at 0.5 of the virial radius. Also shown is the star formation rate for stars forming within 0.5 of the virial radius (black line). For all panels, the star formation rates shown are computed over a 10 Myr time-scale.

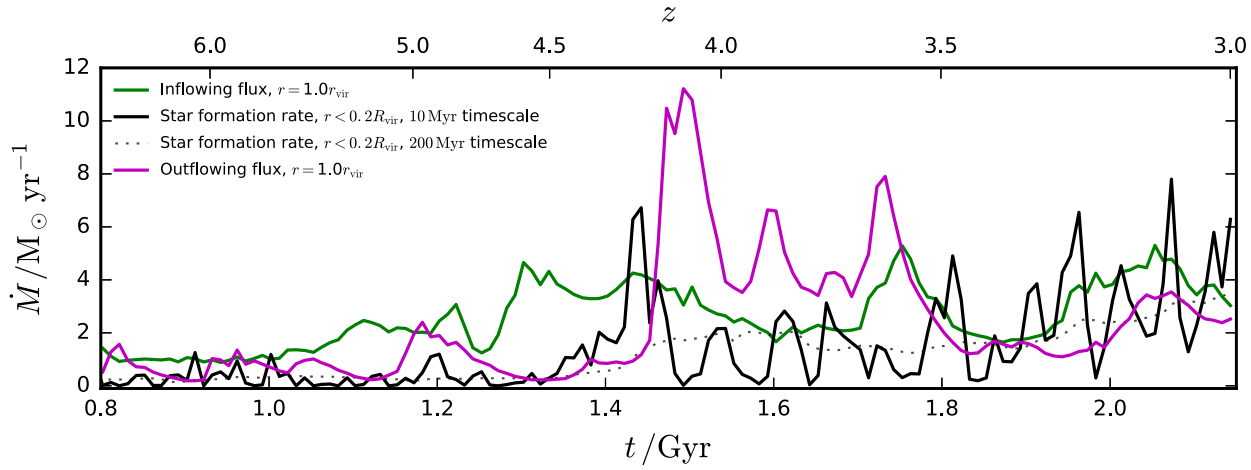

Figure 6. Star formation and flux histories of a simulated halo of mass, $\log(M_{\rm H}/{\rm M}_\odot) = 11.1$ at $z = 3$ (halo 11 in Table 1). Fluxes of inflowing (green) and outflowing (magenta) gas through the virial radius are shown. Also shown is the star formation rate for stars forming within 0.2 of the virial radius, computed over a 10 Myr (solid black) and a 200 Myr (dotted black) time-scale.

relationship between inflow, star formation and outflow, it is also useful to briefly consider a more massive halo. Fig. 6 shows the most massive halo in our sample (halo 11 in Table 1), which has a final mass of $\log(M_{\rm H}/{\rm M}_\odot) = 11.1$ at $z = 3$. Similar to the smaller halo shown in Fig. 5, this halo also exhibits strong short-term fluctuations (tens of Myr) in the star formation rate. The star formation rate computed over a 200 Myr time-scale (as traced by UV starlight) is comparatively smooth in time such that it would be consistently detected in the UV, unlike the smaller halo. While there are still strong mass outflows that leave the halo (magenta line), it can be seen qualitatively that the ratio of integrated outflow to integrated star formation is much smaller in the massive halo (the ratio is of order unity integrated to $z = 3$).

5 HALO BARYON FRACTIONS AND SN FEEDBACK

Fig. 7 shows the baryon fractions of our simulated haloes at $z = 3$. Without feedback (small magenta points), the baryon fractions are typically above the universal value (see the discussion in footnote 6 of Kimm et al. 2015). When supernova feedback is included (black points), the baryon fractions are significantly lowered to below the universal value. The reduction in baryon fractions associated with introducing supernova feedback can be attributed to a combination of two effects. In part, gas is ejected from haloes as an outflow, and in part, the accretion rate of inflowing material is lowered. Most of the haloes are consistent with the distribution of baryon fractions in the EAGLE simulation, indicating that the net efficiency of feedback in removing baryons from haloes is similar. Given that EAGLE produces lower stellar masses (which are better in agreement with extrapolations to abundance matching constraints) than our simulations for $M_{\rm H} > 10^{10.5}\,{\rm M}_\odot$, this underlines that there are more factors at work which determine the efficiency of star formation than just the mass of baryons within the virial radius.

In the following subsections, we investigate the origin of the reduced halo baryon fractions. In Section 5.1, we measure the mass removed by outflows. In Section 5.2, we show that feedback also reduces the accreted mass. In Section 5.3, we show that the decrease in halo baryon fractions corresponds primarily to a reduction of mass in galaxies and has only a small effect on the total mass

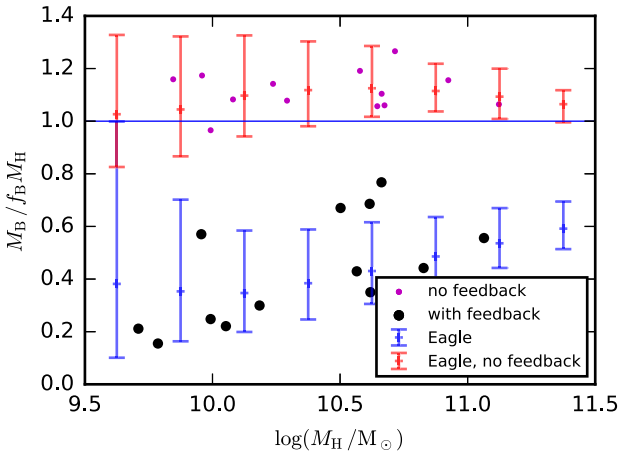

Figure 7. Total baryon mass within the virial radius, $M_{\rm B}$, of simulated central haloes, plotted as a function of halo mass at $z = 3$. Here, baryons considered to be gravitationally bound to satellites are included in $M_{\rm B}$. Baryon masses are normalized by the halo mass, $M_{\rm H}$, scaled by the universal baryon fraction, $f_{\rm B}$. Black points show simulated haloes in runs that include SN feedback. Magenta points show simulated haloes in runs that do not include SN feedback. Blue points show the 10th, 50th and 90th percentiles of the distribution in the reference EAGLE simulation at $z = 3$, including only central objects. Red points show the corresponding distribution for an EAGLE simulation without feedback. The blue horizontal line marks an enclosed baryon fraction of unity, where the baryon fraction inside the halo is equal to the universal value. For both Eagle and our simulated haloes, the halo virial radius is defined as the radius at which the enclosed average density is equal to 200 times the critical density of the universe.

in the CGM. We then explore the CGM mass budget split into outflowing/inflowing neutral/ionized components.

5.1 Outflow masses and loading factors

The relationship between star formation and mass outflows is demonstrated anecdotally in Figs 5 and 6. To quantify this effect for our full sample, we introduce an integrated loading factor,

$$\eta_{\rm int}(r,t) \equiv \frac{\int_0^t \dot{M}_{\rm out}(r(t'),t')\,{\rm d}t'}{\int_0^t \dot{M}_\star(<r(t'),t')\,{\rm d}t'}, \qquad (10)$$

where $\dot{M}_\star(<r(t'),t')$ is the star formation rate interior to a radius, $r(t')$, at a time t', and $\dot{M}_{\rm out}(r(t'),t')$ is the mass flux of radially outflowing gas passing through a surface[9] at a radius, $r(t')$, at time, t'. Hence, $\eta_{\rm int}(r,t)$ represents the ratio of integrated mass outflow to integrated star formation and, as such, can be considered as an (integrated) efficiency of feedback. We prefer to use this quantity when assessing the efficiency of feedback rather than an instantaneous mass-loading factor ($\eta_{\rm ml} \equiv \dot{M}_{\rm out}/\dot{M}_\star$) to reduce the systematics and noise associated with variability and phase offsets between star formation and outflow, as seen in Figs 5 and 6. To give an idea as to the importance of these effects, and to give a quantity which can be readily compared to observations, we also consider the instantaneous mass-loading factor, $\eta_{\rm ml}$, with $\dot{M}_\star$ computed over a 200 Myr time-scale (so as to be comparable to star formation rates estimated from the UV continuum).

We also consider the outflow mass, defining

$$M_{\rm out}(r,t) \equiv \int_0^t \dot{M}_{\rm out}(r(t'),t')\,{\rm d}t', \tag{11}$$

as the integrated mass in gas that passes radially outwards through a surface at $r(t')$.

In Fig. 8, we plot the instantaneous (top) and time-integrated loading factors (middle panel) of our targeted, simulated haloes as a function of halo mass for two different surfaces at 0.5, 1 $R_{\rm Vir}$. As expected, there is significant scatter in the distribution of instantaneous mass-loading factors. The scatter is smaller if we instead consider the time-integrated loading factors. In this case, the loading factors are virtually identical between the two surfaces (red and black points), meaning that mass outflows driven by SN propagate all the way through, and out of, the halo (regardless of the halo mass). The absolute value of the integrated loading factor scales with halo mass, ranging from values of $\eta_{\rm int} \sim 15$ at $M_{\rm H} = 10^{10}$ M$_\odot$ to $\eta_{\rm int} \sim 1.5$ at $M_{\rm H} = 10^{11}$ M$_\odot$.

The amount of outflowing mass can be seen in an absolute sense by considering the bottom panel of Fig. 8, which instead shows the integrated outflowing masses, $M_{\rm out}$, normalized by the final halo mass at $z = 3$. Here, we see that relative to the expected baryonic growth of the halo ($f_{\rm B}M_{\rm H}(z=3)$), the outflows expel somewhere between 20 and 60 per cent of the expected baryonic mass out of the halo. Normalized in this way, there appears to be no trend with halo mass. This indicates that the mass dependence of the baryon fractions shown in Fig. 7 is caused by an effect other than outflows removing mass from haloes. Comparing the time-integrated outflow rates shown in the lower panel of Fig. 8 to the halo baryon fractions shown in Fig. 7, it is apparent that outflows alone do not account for the low baryon fractions seen when SN feedback is included: we find that outflows from the central galaxies contribute to between ∼20 per cent and ∼60 per cent of the reduction in baryon fractions.[10]

Notably, there are two simulated haloes (the third and seventh most massive) that appear to have unusually low integrated loading factors compared to the trend outlined by the rest of the sample (these are haloes 5 and 9 in Table 1). These are (not coincidentally) the two haloes that have the highest ratio of $M_\star/M_{\rm H}$ in Fig. 3. We see in the bottom panel of Fig. 8 that these haloes do not have unusually low integrated outflow masses relative to the rest of the sample. This indicates that these outliers in the integrated loading

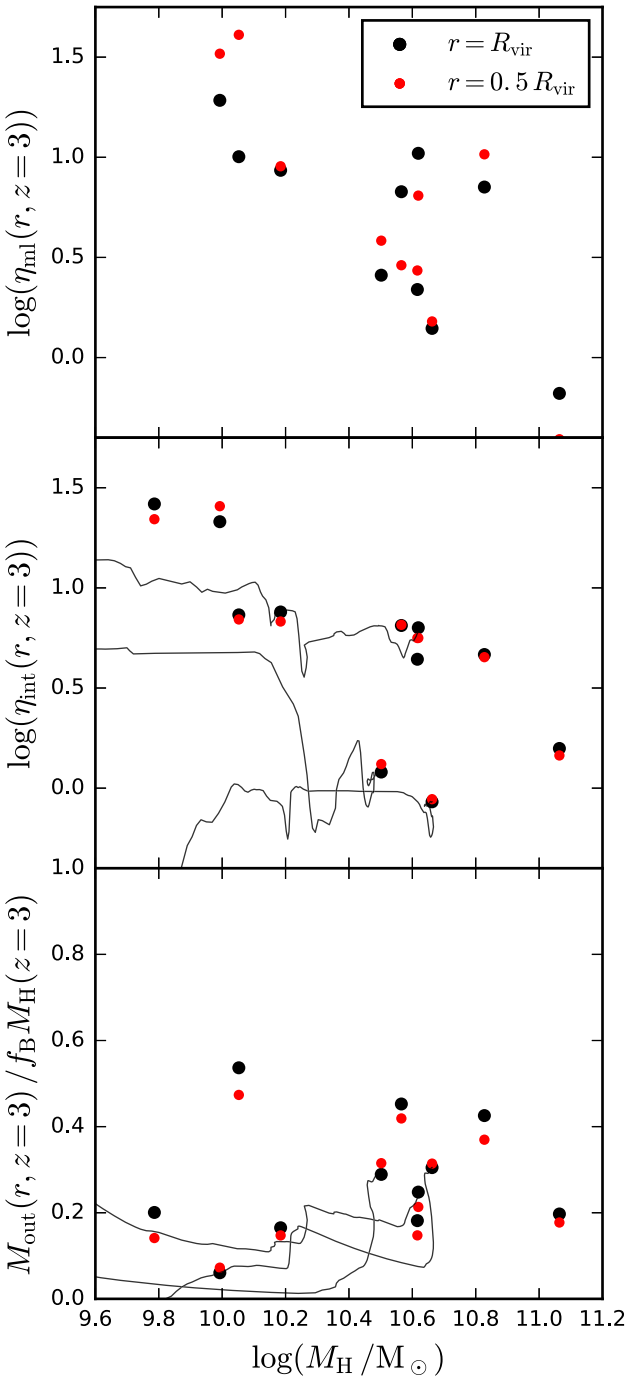

Figure 8. *Top:* instantaneous mass-loading factor, $\eta_{\rm ml}(r,t)$, plotted as a function of halo mass for the haloes simulated with SN feedback. Only the central main-target haloes for the 11 zoom simulations are shown. Star formation rates used for this quantity are computed over a 200 Myr time-scale. Red points show the loading factor for a surface placed at half the halo virial radius. Black points show the loading factor for a surface placed at the halo virial radius. *Middle:* same as the top panel but showing instead the time-integrated loading factor, $\eta_{\rm int}(r,t)$. The loading factors are computed by integrating down to $z = 3$. Black lines show past tracks for three example objects, with the time integral performed up to the time that a halo has a given mass. *Bottom:* same as the top panel but instead plotting the normalized, time-integrated outflow mass. The normalization factor is the baryonic mass at the halo would have at $z = 3$ if it contained the universal baryon fraction. For the past tracks in this panel (black lines), the halo mass used is the instantaneous halo mass.

[9] In practice, we always place the surface at a fraction of the halo virial radius, for example at $r(t') = 0.5R_{\rm vir}(t')$.
[10] This can be seen cross-referencing Fig. 7 with Fig. 8.

factor distribution are caused by unusually efficient star formation. The two galaxies are not unusual in their stellar specific angular momentum or half-mass radii with respect to the rest of sample so this difference does not appear to be caused by above average compactness. The black lines in Fig. 8 show the past tracks for these two outlying haloes (as well as a third, non-outlier halo as a reference). The more massive outlier (halo 9, also the halo for which feedback has almost no effect on the stellar mass) has a persistently low time-integrated loading factor (middle panel) and experiences significant outflows only relatively late in the haloes growth history (bottom panel). The less massive outlier (halo 5) undergoes very little early star formation (and hence outflows), with most of the stars formed in two large bursts around $z = 4$, leading again to an abrupt increase in outflowing mass (after which the halo does not grow significantly in mass, bottom panel).

5.2 Inflows and SN feedback

A second factor that can affect halo baryon fractions is the inflow rate of gas. Substituting the outflowing mass flux, $\dot{M}_{\rm out}(r(t'), t')$ with the inflowing mass flux, $\dot{M}_{\rm in}(r(t'), t')$, in equation (11), we define the time-integrated inflow mass, $M_{\rm in}$. For inflow, we choose to start the time integral at $z = 8$ because we do not have sufficient simulation outputs to accurately quantify the amount of inflow at early times. Fig. 9 (top panel) shows $M_{\rm in}$, integrated from $z = 8$ down to $z = 3$ for two surfaces and for simulations with and without SN feedback. Roughly speaking, the same amount of gas that enters the virial radius also crosses the inner surface at $0.5\,R_{\rm vir}$, although this is complicated by gas stripping from satellites. We note here that the UV background does not impact the inflow of gas on to haloes in the halo mass range shown (this effect becomes relevant for $M_{\rm H} \leq 10^9\,{\rm M}_\odot$; Gnedin 2000; Iliev et al. 2007; Wise et al. 2014; Oñorbe, Hennawi & Lukić 2017).

Interestingly, there is a difference between the simulations with and without SN feedback. This difference is made more explicit in the bottom panel of Fig. 9 which shows the ratio of points in the top panel by matching haloes between simulations with and without feedback. This shows that relative to the no-feedback case, there can be 20–80 per cent less gas accretion on to, and within, haloes that are simulated with SN feedback. The trend appears to be mass-dependent, such that inflow rates in the lower mass haloes from our sample are more affected by feedback. This trend leads to the mass-dependent halo baryon fractions shown in Fig. 7. The reduction in gas accretion rates due to feedback explains ∼30–50 per cent of the total reduction in halo baryon fractions. Note that we have normalized away the difference in final halo mass to account for the fact that in simulations with feedback, haloes are less massive (see Schaller et al. 2015, for a more general discussion of this effect). Without normalizing in this way, the impact of feedback on inflow rates would be even more pronounced.

We have shown that outflows (inflows) contribute ∼20–60 per cent (∼40 per cent) to the reduction in halo baryon fractions. The remaining 0–50 per cent reduction in halo baryon fractions is caused by a reduction in the baryon fractions of satellites before they are accreted on to the central haloes.

5.3 CGM mass budget

Following the compartmentalization scheme introduced in Section 2.6, Fig. 10 compares the mass in the CGM to the gas mass in satellites and the central galaxy. When SN feedback is included (black points), the mass in the CGM (inflows + outflows) is comparable to

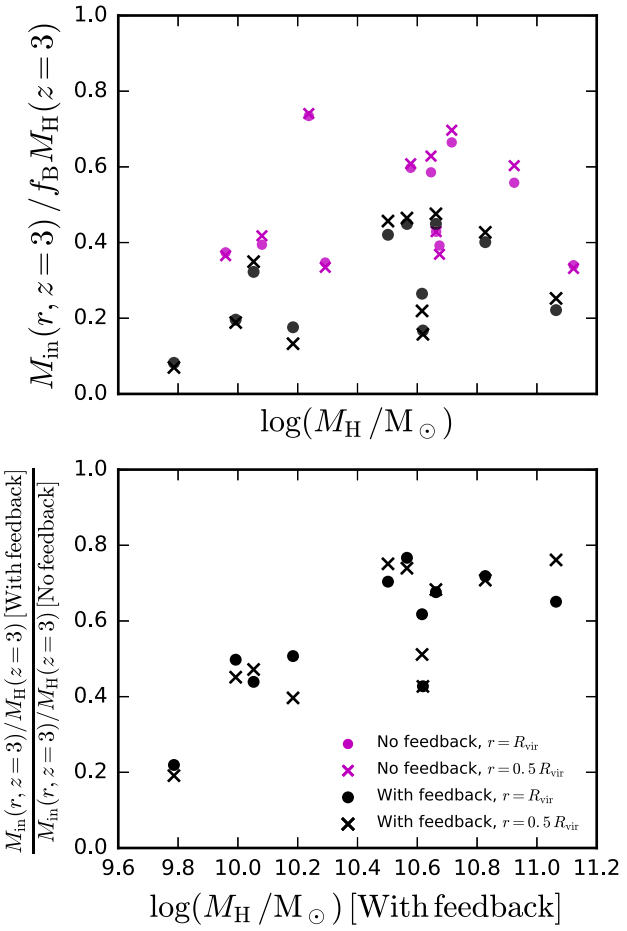

Figure 9. *Top:* normalized, time-integrated inflow mass, plotted as a function of halo mass for haloes simulated with SN feedback. The normalization factor is the baryonic mass the halo would have if it contained the universal baryon fraction. Inflow masses are computed by integrating the inflowing mass flux from $z = 8$ down to $z = 3$. Gas which is considered gravitationally bound to satellites is excluded. Only the central main-target haloes for the 11 zoom simulations are shown. Star formation rates used for this quantity are computed over a 200 Myr time-scale. Magenta points show simulations without SN feedback. Black points show simulations with SN feedback. Crosses show $M_{\rm in}(r = 0.5\,R_{\rm vir})$, the inflow through a surface at half the virial radius. Circles show $M_{\rm in}(r = R_{\rm vir})$, the inflow through a surface at the virial radius. *Bottom:* the ratio of the points in the top panel, matching haloes between simulations with and without SN feedback.

the gas mass in the central galaxy.[11] The fraction of mass in satellites exhibits a substantial scatter but is typically comparable to (or greater than) the mass in the CGM or the central galaxy. Normalized by the final halo mass at $z = 3$, there are no obvious trends in the compartmentalization of baryons with halo mass.

While Fig. 7 shows that including supernova feedback typically reduces the net baryon content inside haloes by half at $z = 3$, Fig. 10 shows that this change is primarily associated with a reduction in the mass of the central galaxy (and from satellites to a lesser extent). The total CGM typically contains slightly more mass when feedback is included, mostly because the outflowing component is significantly enhanced. The increase in the mass of outflows is still

[11] The two outliers (black points with $M_{\rm galaxy}/f_{\rm B}M_{\rm H} > 0.3$) are haloes 5 and 9 (see Table 1), the two outliers with unusually high stellar masses and low integrated loading factors shown in Figs 3 and 8.

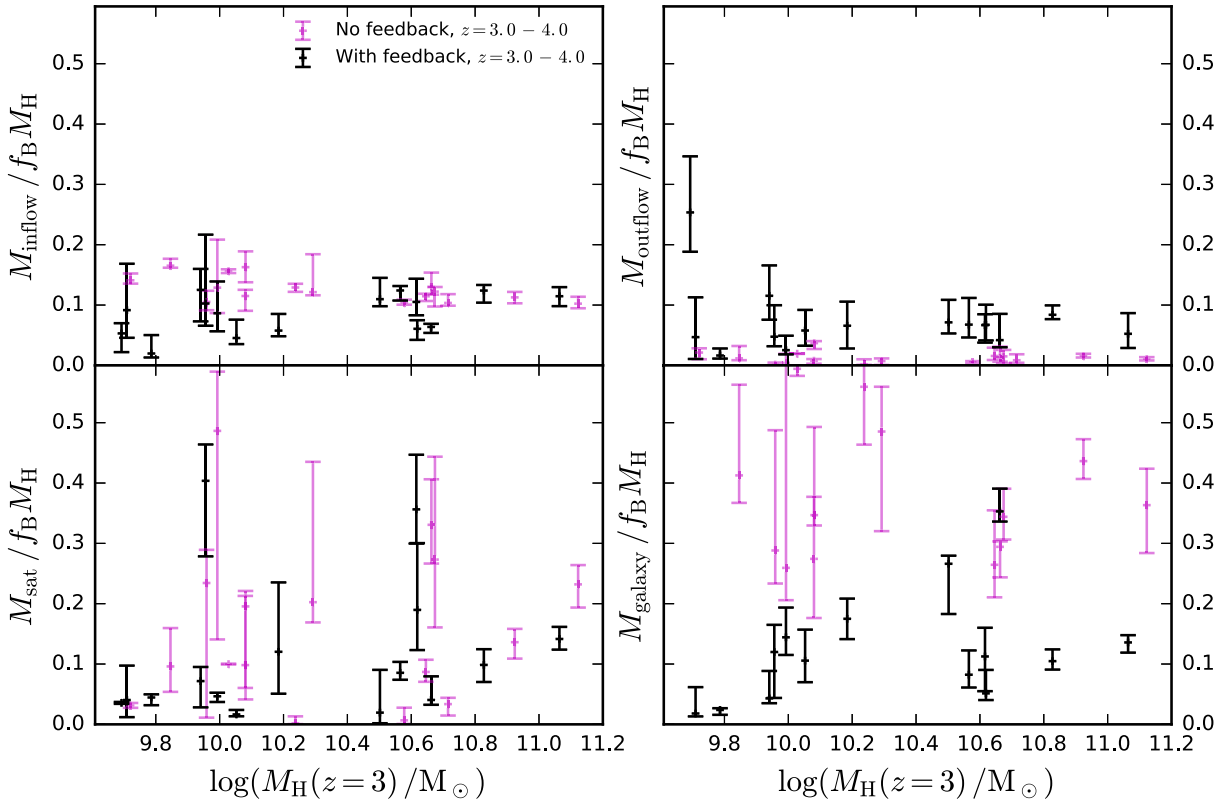

Figure 10. Gas mass associated with the inflowing CGM, $M_{\rm inflow}$, the outflowing CGM, $M_{\rm outflow}$, satellites, $M_{\rm sat}$, and the central galaxy, $M_{\rm galaxy}$, plotted as a function of halo mass for central galaxies at $z = 3$. Each panel corresponds to a different baryonic component, as labelled. Points and errorbars show the distribution (16th, 50th and 84th percentiles) of component masses over a range of redshifts ($z = 3$–4) for a single simulated halo. Black points show haloes for simulations that include SN feedback. Magenta points show haloes simulated without SN feedback. The normalization factor $f_{\rm B}\,M_{\rm H}$ is the baryon mass each halo would have if it contained the universal baryon fraction.

modest compared to the decrease in the mass of galaxies. This is because most of the outflowing gas moves with very high velocities, quickly leaving the halo.

Interestingly, the reduced accretion rates discussed in Section 5.2 do not translate into a significantly reduced mass of inflowing gas in the CGM. Instead, SN feedback reduces inflow rates primarily by reducing the radial velocity of inflowing warm/hot ionized gas by up to a factor 2 (not shown). As such, less mass is accreted on to the CGM but the gas which is accreted spends a longer time (on average) in the CGM before infalling on to the central galaxy. The average radial velocity of the neutral inflowing phase is also reduced but by a lesser amount.

From an observational perspective, we are interested in understanding how the *neutral* CGM is affected by feedback, as this is the gas traced by Ly$\,\alpha$, both in absorption and emission. Fig. 11 shows how the mass of hydrogen in the CGM is divided between inflowing/outflowing and neutral/ionized phases for redshifts in the range $3 < z < 4$. The mass in ionized hydrogen (left-hand panels) is typically a factor 5 larger than the mass in neutral hydrogen (right-hand panels) for this redshift range. Also, the inflowing mass is about a factor 2 larger than the outflowing mass for both neutral and ionized phases, even when feedback is included. These results do not appear to depend on halo mass.

Looking at the right-hand panels of Fig. 11, we see that SN feedback in our simulations does not significantly increase the mass of outflowing H I in the CGM. The increase in the outflowing mass of the CGM is instead almost entirely due to an increase in the mass in ionized outflow. SN feedback does increase the mass of inflowing H I by a factor ∼2. Put together, this suggests that the effect of feedback should be visible through H I emission or absorption. However, our results suggest that most of the signal will come from inflowing gas, which makes a quantitative interpretation of such observables extremely challenging.

The origin of the enhanced inflowing H I content is not clear. It may reflect a conversion of inflowing ionized hydrogen into the neutral phase. Alternatively, if feedback slows the inflowing neutral gas without changing the accretion rate through the virial radius, the mass of this CGM component will be increased. As discussed previously, we indeed find that the average radial velocity of inflowing neutral gas is reduced slightly by feedback.

6 RADIAL PROFILES AND GAS FLOWS IN THE CGM

Here, we explore the radial dependence of various CGM properties by stacking haloes in the halo mass range, $10.5 < \log(M_{\rm H}/{\rm M}_\odot) < 11.2$, over the redshift interval, $3 < z < 4$ (we explore other mass/redshift ranges in Appendix A). Stacking yields a complete statistical description of how inflows and outflows cross the CGM, averaging over the strongly fluctuating inflow and outflow rates at a given radius (see Fig. 5). This allows us to address questions such as whether outflows in a given gas phase conserve mass as they propagate radially outwards (without needing the Lagrangian information provided by particle-based hydrodynamic codes or tracer particles). Haloes are mean stacked, changing the radius variable from r to $r/R_{\rm vir}$ and weighting simulation outputs such

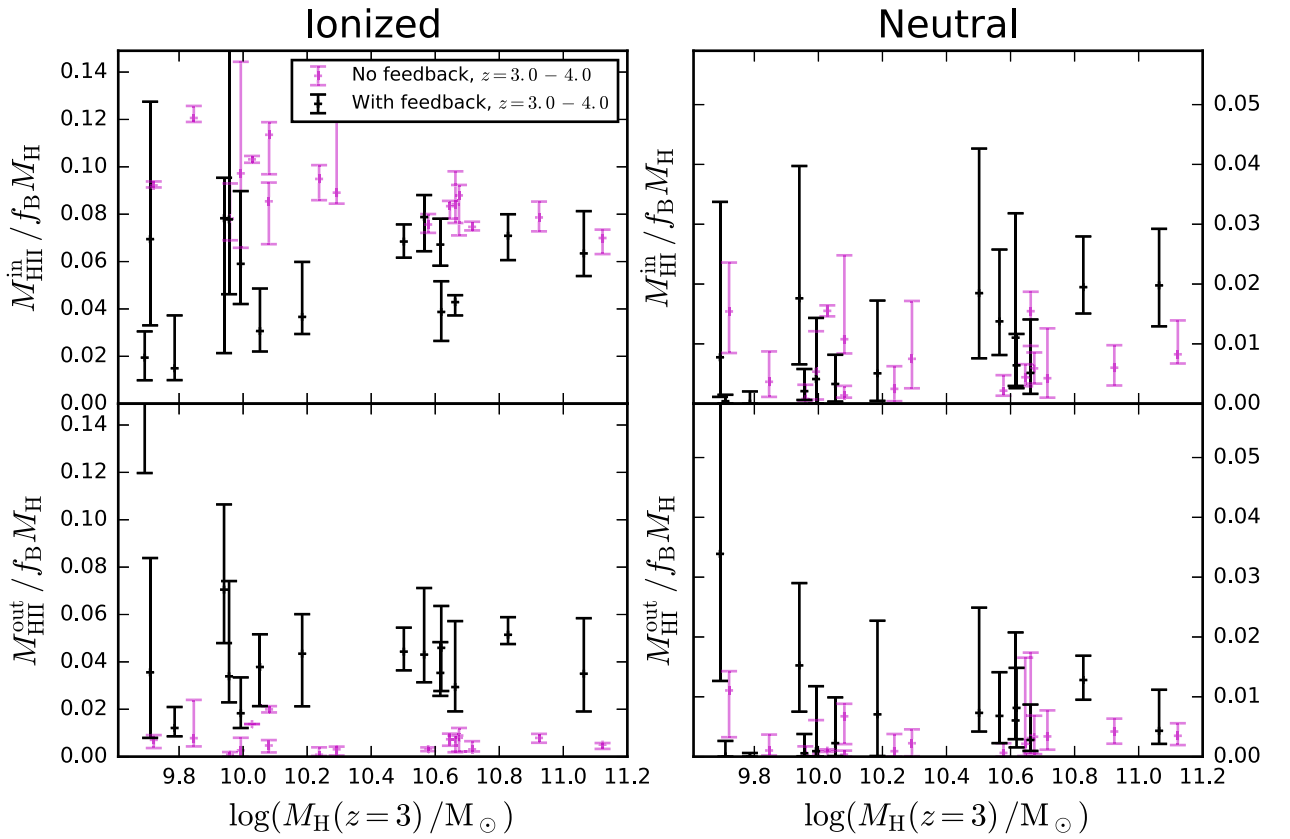

Figure 11. Normalized hydrogen mass in different circumgalactic gas components, plotted as a function of halo mass for central galaxies at $z = 3$. These components include inflowing ionized hydrogen (top-left), inflowing neutral hydrogen (top-right), outflowing ionized hydrogen (bottom-left) and outflowing neutral hydrogen (bottom-right). Note that the dynamic range in the y-axis of the panels showing neutral hydrogen is significantly reduced compared to the panels showing ionized hydrogen. Points and errorbars show the distributions (16th, 50th and 84th percentiles) of component masses over a range of redshifts ($z = 3$–4) for a single simulated halo. The errorbars therefore indicate the time variability in the component mass for each halo over this redshift range. Black points show haloes for simulations that include SN feedback. Magenta points show haloes simulated without SN feedback. The normalization factor $f_{\rm B}\,M_{\rm H}$ is the baryon mass each halo would have if it contained the universal baryon fraction.

that haloes with different numbers of simulation outputs contribute equally to the stack. Our stacking window (600 Myr) is sufficiently large as to capture at least a single crossing of any of the gas components which we consider.

Fig. 12 shows the mean stacked, spherically averaged radial profiles of mass and metallicity (defined as the ratio of metal to total gas radial mass profiles). While satellites are removed, we do not attempt to subtract material from the central galaxy from these profiles. Roughly speaking, the cold ISM of the central galaxy can extend out to $\sim 0.2\,R_{\rm vir}$, and so the profiles out to these radii should be interpreted accordingly.

Comparing to the integrated masses presented in Figs 10 and 11, several of the same features are apparent in Fig. 12. There is systematically more mass in inflows than in outflows at all the radii considered. This is also true for the neutral and warm-ionized gas phases (blue and green lines, respectively). The hot-ionized phase contains more mass in outflow than in inflow. Comparing the mass between the different phases, ionized hydrogen (warm plus hot) in the CGM dominates over neutral hydrogen away from the central galaxy ($r \gtrsim 0.2\,R_{\rm vir}$). Away from the central galaxy, hot-ionized hydrogen dominates the outflowing mass. For the inflowing CGM, however, the cooler warm-ionized phase contains the majority of the mass, particular in the inner CGM ($r < 0.6\,R_{\rm vir}$).

Alongside the radial mass profile, the metallicity profile contains highly complementary information. Outflowing gas has systematically higher metallicity than inflowing gas for all of the phases shown. Among the various outflowing phases, hot-ionized hydrogen is the most metal rich and neutral hydrogen is comparatively metal poor. The total metallicity of outflow (grey solid line) is fairly constant with radius, whereas the metallicity of inflow (dashed grey line) drops by over an order of magnitude from $0.1\,R_{\rm vir}$ to $R_{\rm vir}$.

In order to interpret further the information contained in the radial profiles shown in Fig. 12, we note the two following points. First, the CGM in our simulations is not in a quasi-hydrostatic configuration. Rather, all of the gas phases shown exhibit significant radial velocities. The radial mass profiles should thus be interpreted in terms of mass fluxes rather than as an equilibrium solution. Secondly, the radial velocity gradients of different phases are too small to explain several of the features present in the radial mass profiles of Fig. 12 (see Fig. 14). Instead, to zeroth order these radial mass profiles can be interpreted assuming the gas moves with constant radial velocities.[12]

[12] Note that formally written as a continuity equation the appropriate radial profile to consider for mass conservation is the radial momentum profile (which factors in changes of the gas radial velocity). Qualitatively, the radial momentum (not shown here) and radial mass profiles shown in Fig. 12 are identical. This confirms that velocity changes indeed play a minor role in shaping the radial mass profiles.

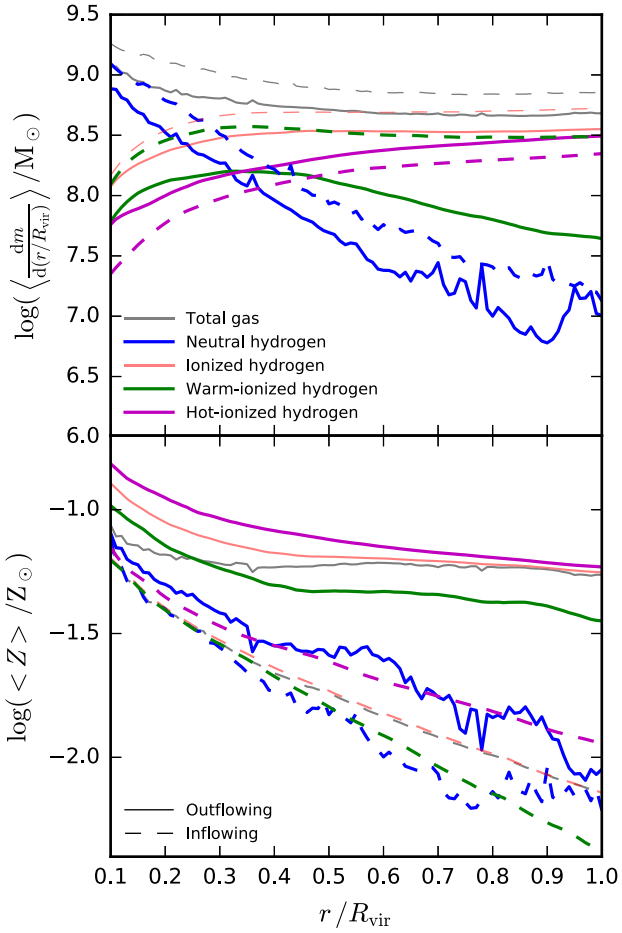

Figure 12. Spherically averaged radial profiles of mass (top) and metallicity (metallicity). Solid lines show the profiles for gas that is radially outflowing. Dashed lines show the profiles for gas that is radially inflowing. Black lines show the total gas, red lines show ionized hydrogen and blue lines show neutral hydrogen. Green and magenta lines show ionized hydrogen subdivided between warm and hot phases, separated at $T = 10^{4.5}$ K. The profiles are computed by taking the mean over seven haloes, simulated with SN feedback, with mass $10.5 < \log(M_{\rm H}/{\rm M}_{\odot}) < 11.2$, using all of the available simulation outputs (15 Myr spacing) over the redshift range, $3 < z < 4$. This redshift interval corresponds to a time interval of $\Delta t \sim 600$ Myr.

Fig. 13 shows a cartoon which guides the interpretation of Fig. 12. A zero gradient for the sum of inflowing (or outflowing) phases (grey lines in Fig. 12) implies that there is zero net mass exchange between inflowing and outflowing components, which is compatible with a scenario where gas elements cross the entire halo without reversing direction. Non-zero but equal gradients for outflow and inflow imply turnaround, such that a fraction of gas elements reverse direction over the stacking time window. Negative radial gradients indicate mass leaving the galaxy that falls back at a later time. Correspondingly, positive radial gradients indicate mass that inflows through the virial radius but is ejected from the halo at a later point.

Fig. 12 shows that the radial mass profiles of both inflowing and outflowing gas (grey solid and dashed lines) are flat for $0.6 < r/R_{\rm Vir} < 1$ but show negative gradients over the radial range, $0 < r/R_{\rm Vir} < 0.6$. We have verified that these radial gradients $(\frac{\rm d}{{\rm d}(r/R)}\frac{{\rm d}m}{{\rm d}(r/R)})$ are almost equal for the inflowing and outflowing components. This therefore implies that some fraction of the mass which outflows from the halo centre turns around inside $0.6R_{\rm Vir}$ and joins the inflowing component. This picture is supported by the

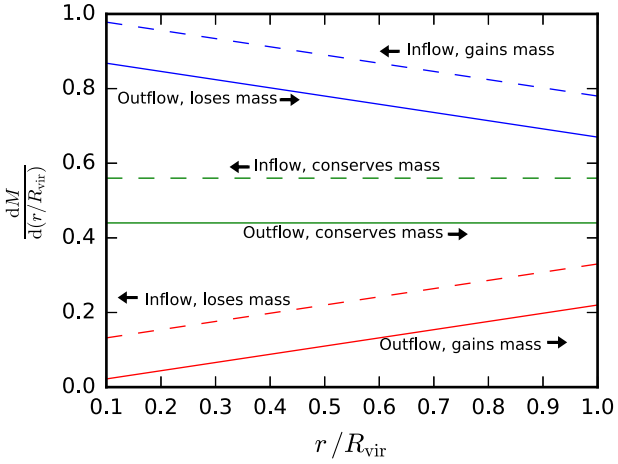

Figure 13. Cartoon schematic demonstrating the relationship between radial mass profiles and mass conservation. If inflowing (dashed lines) and outflowing (solid lines) components move with a constant radial velocity, the gradients of the radial mass profiles can be interpreted as indicators of mass conservation. If no mass exchange between inflow and outflow occurs, mass is conserved and the gradients of the radial mass profiles are zero (green lines). If outflow net loses mass to inflow as it propagates outwards, the radial mass profiles have negative gradients (blue lines). Conversely, if inflow net loses mass to outflow as it propagates inwards, the radial mass profiles have positive gradients (red lines). Note that this schematic does not consider separate gas phases. For an individual gas phase, gradients in the radial mass profile depend on the rate of mass exchange between both inflowing and outflowing phases.

metallicity profile shown in the lower panel of Fig. 12. The metallicity of inflowing gas entering the halo is significantly lower than the metallicity of outflowing gas leaving the galaxy. As such, the large negative radial metallicity gradient for inflowing gas indicates that there must be exchanges between the outflowing and inflowing components.[13]

Focusing on the neutral phase of hydrogen (blue lines), Fig. 12 shows a strong negative gradient for the mass profile over the entire radial range considered. This means that outflowing neutral hydrogen is not conserved in mass as it flows outwards through the halo. The inflowing neutral phase shows a corresponding negative gradient. A straightforward explanation for this is that a fraction of the neutral outflow loses radial kinetic energy climbing out of the gravitational potential, rejoining the inflowing component in a galactic fountain process. Another possibility is that mass exchange occurs between the neutral outflow and other ionized phases (either inflowing or outflowing), such that the neutral material is lost due to photoionization/collisional ionization.

Turning our attention to the inflowing phases, Fig. 12 shows that mass is continually lost from the hot-ionized phase as it flows further into the halo, the warm-ionized gas is approximately conserved and the neutral phase continually gains mass. Again, this can be contributed to by both mass exchanges between outflowing and inflowing components as well as mass exchanges between different phases within the same component.

Put together, we find that no inflowing/outflowing phase is mass conserving: none of the curves in the upper panel of Fig. 12 are flat.

[13] Note that the total radial metallicity profile of outflowing gas (solid grey line in Fig. 12) is flat because of the combination of metallicity segregation between different outflowing gas phases and the changing relative mass fractions of those phases as a function of radius.

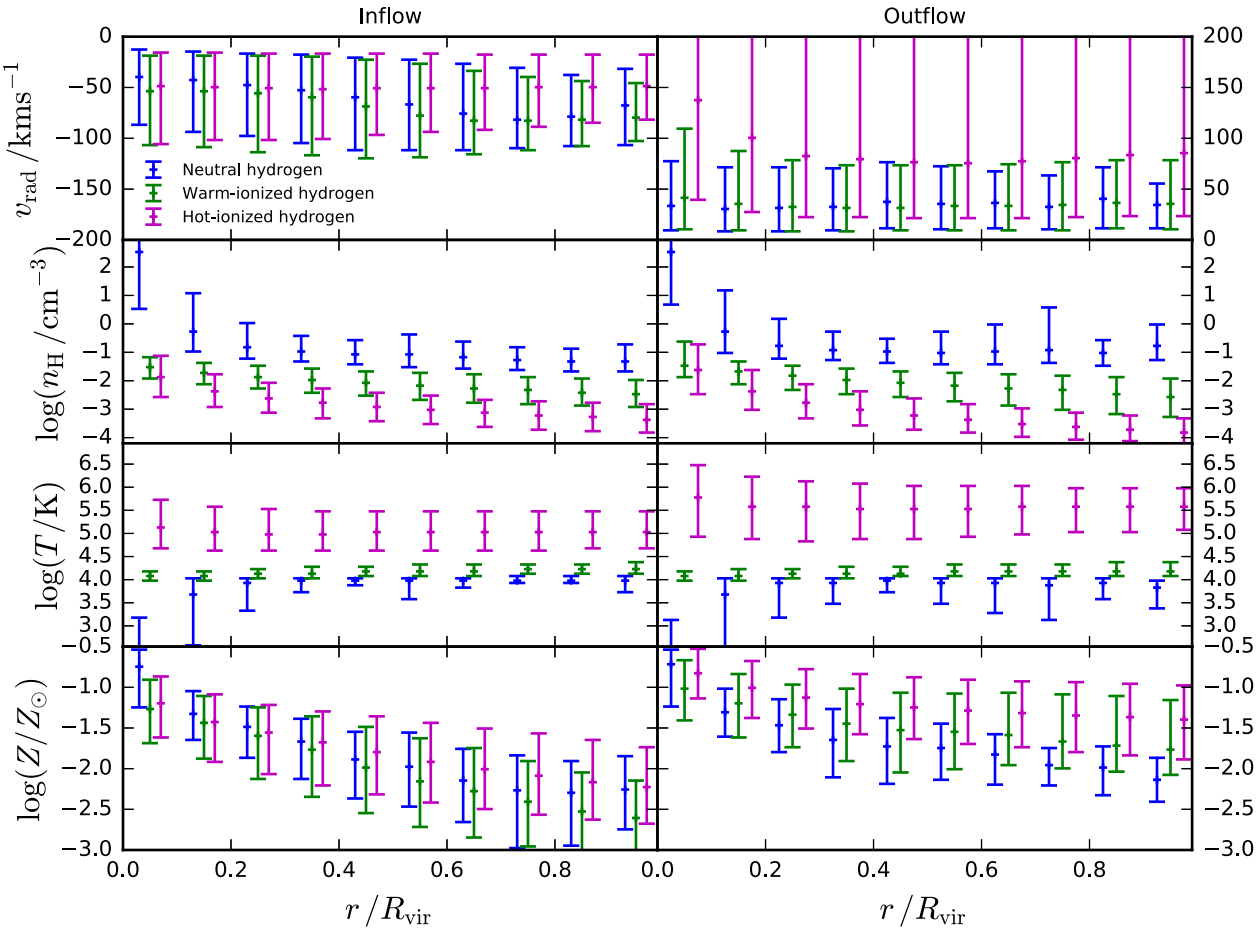

Figure 14. Distributions of local gas properties plotted as a function of radius, computed by stacking haloes, simulated with SN feedback, with mass $10.5 < \log(M_{\rm H}(z=3)/{\rm M}_\odot) < 11.2$ over the range $3 < z < 4$. The left and right columns show distributions for inflowing and outflowing gas, respectively. Gas properties shown include radial velocity (top), density (second row), temperature (third row) and metallicity (bottom). Gas cells considered gravitationally bound to satellites are not included. The blue, green and magenta points show the mass-weighted 16th, 50th and 84th percentiles of the distributions for neutral, warm-ionized and hot-ionized phases of hydrogen, respectively.

Moreover, different gas phases exhibit very different behaviour with respect to each other. If these results are representative of real galaxies, the inference of outflow properties from absorption line measurements (both down-the-barrel and from background quasars) becomes challenging. Specifically, there is a common assumption that outflows in a given phase conserve mass (e.g. Bouché et al. 2012; Heckman & Thompson 2017), although see Chisholm et al. (2017) for a counter-example.

6.1 Local gas properties

Fig. 14 shows the local properties of the CGM, divided into different phases of inflowing/outflowing hydrogen. Histograms and percentiles are again computed by stacking haloes in the same manner as for Fig. 12. Fig. 14 shows the inflowing gas does not exhibit evidence of any radial acceleration as it falls further into the halo. Rather, the inflowing warm-ionized and neutral phases radially decelerate slightly for $r < 0.5R_{\rm vir}$ (note that the tangential velocity increases accordingly). Outflowing neutral and warm-ionized hydrogen moves with fairly modest radial velocities, independent of radius. On average, hot-ionized outflowing material moves much faster by comparison and with a much broader radial velocity distribution.

For both inflowing and outflowing components, warm-ionized, hot-ionized and neutral phases of hydrogen clearly segregate in density and temperature (by construction for the hot/warm divide). Comparing neutral inflow and outflow, it is interesting that neutral outflowing hydrogen has broader density and temperature distributions, indicating that part of this phase is more associated with clumps while neutral inflow is more diffuse on average. This can be seen visually in Fig. 2. This difference between neutral inflow and outflow disappears at higher redshifts ($z \geq 4$, not shown), with the neutral outflow instead showing a narrower density distribution similar to the inflowing neutral hydrogen density distribution shown in Fig. 14 for lower redshift.

The metallicities of different inflowing phases are fairly similar to each other while the metallicities of outflowing phases are more segregated. For outflowing gas the level of metallicity segregation between different phases does not decrease with increasing radius (rather the opposite), implying that different outflowing phases do not significantly mix with each other as they propagate outwards. For inflowing gas, metallicities rise strongly as gas moves towards the centre. This may be the result of a galactic fountain in which enriched outflowing gas falls back on to the galaxy. Alternatively, gradual metal enrichment of the inflowing gas occurs through mixing with the enriched outflowing phases. In practice, both processes presumably occur.

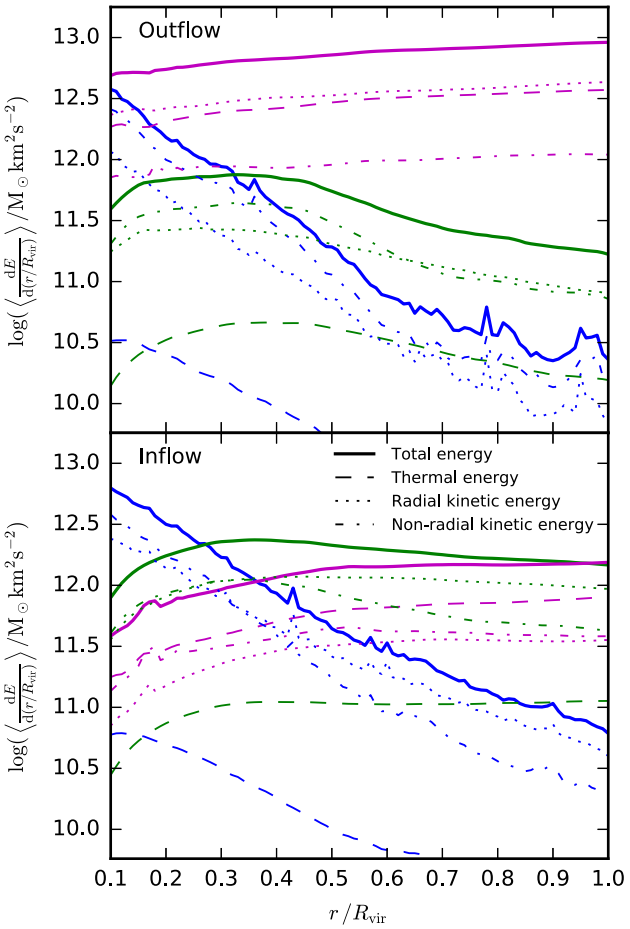

Figure 15. Spherically averaged radial profiles of energy, plotted as a function of radius inside haloes. The profiles are separated between radially outflowing (top panel) and inflowing (bottom panel) gas. The profiles are further separated between neutral (blue lines), warm-ionized (green) and hot-ionized (magenta) phases of hydrogen. Solid lines show total energy (thermal plus kinetic). Dashed lines show thermal energy. Dotted lines show kinetic energy associated with radial motion. Dash–dotted lines show the remaining kinetic energy associated with non-radial motion. The halo sample and stacking time interval are the same as Fig. 12.

6.2 Energy decomposition of inflow/outflow

Additional information on the nature of gas flows in our simulated haloes is shown in Fig. 15, which shows the decomposition between radial-kinetic, tangential-kinetic and thermal energy for the same halo stack as in Fig. 12. Outflowing hot-ionized hydrogen dominates in energy and is clearly comprised of a coherent, thermalized radial outflow. In contrast, the warm-ionized outflow contains negligible thermal energy and a comparable amount of radial-kinetic and tangential-kinetic energy. The neutral outflow contains systematically more tangential-kinetic energy for most of the radial range considered. This shows that the warm-ionized and neutral outflowing CGM is not in a coherent radial wind, and instead exhibits a more complex velocity structure.

Focusing instead on inflows, Fig. 15 shows that as inflowing gas approaches the halo centre, radial-kinetic energy is transferred to tangential-kinetic energy. For the neutral and warm-ionized phases, tangential kinetic energy is the largest contributor to the total energy of these inflowing phases in the inner regions ($r < 0.4\,R_{\rm Vir}$). This is consistent with the slight radial deceleration seen in Fig. 14 for inflowing warm-ionized and neutral hydrogen in this radial range.

6.3 How does SN feedback shape radial mass flows in the CGM?

Expanding on the spatially integrated analysis presented in Section 5.3, the impact of SN feedback on the CGM is shown in more detail in Fig. 16, which compares stacked radial mass profiles between simulations with and without feedback. Consistent with Fig. 11, over the redshift interval, $3 < z < 4$, the stacked neutral hydrogen mass increases in the CGM at all radii when feedback is included (aside from close to the halo centre).

For outflowing neutral hydrogen, the enhancement is modest, showing supernova feedback does not significantly alter the radial mass distribution in this component for this redshift/mass interval.[14] On the other hand, the high-density ($n_{\rm H} > 1\,{\rm cm}^{-3}$) and low-temperature ($T < 4000\,{\rm K}$) part of the outflowing neutral component seen in Fig. 14 is only seen when SN feedback is included. This implies that SN feedback does result in a clumpier outflowing neutral CGM.

Over the higher redshift interval ($4 < z < 6$) shown in the bottom panels of Fig. 16, the inclusion of feedback has a much more significant effect in enhancing the mass of neutral outflowing hydrogen. The mass in inflowing neutral hydrogen is also enhanced by feedback (both relatively and absolutely) in the higher redshift interval, as in the $3 < z < 4$ interval. Unlike the outflow case, neutral inflow is more significantly enhanced in the lower redshift interval.

7 DISCUSSION

7.1 Implications for spatially extended Ly α emission

In future work, we plan to utilize the simulations presented here coupled with radiative transfer calculations to explore the implications of the recently observed, spatially extended Ly α emission around individual faint, high-redshift galaxies (Wisotzki et al. 2016). A key application of such observations is that they are presumably sensitive (at some level) to the details of SN feedback, offering an alternative to analyses of H I covering fractions inferred using absorption from background quasars (which suffer from limited statistics and the difficulty of linking absorbers to galaxies).

Here, we have demonstrated that the inclusion of supernova feedback both significantly reduces the gas content of simulated central galaxies and increases the neutral CGM content. Both these effects are expected to enhance the spatially extended Ly α signal. Decreasing the neutral gas content at the centre of the halo is expected to increase the escape fraction of Ly α photons emitted around young stars in the central galaxy, increasing the number of photons that can be scattered from CGM gas. A competing effect however is the reduction of star formation associated with the inclusion of feedback. Enhanced neutral gas content in the CGM will both increase the amount of direct Ly α emission from the CGM (cooling radiation, fluorescence) and lead to increased scattering further away from any central source of Ly α photons.

Fig. 2 illustrates the typical projected spatial configuration of neutral inflowing and outflowing gas. Inflowing gas is anisotropically

[14] Note that for simulations without feedback, outflowing material stripped from satellites and material moving past pericentric passage can still form an outflowing component.

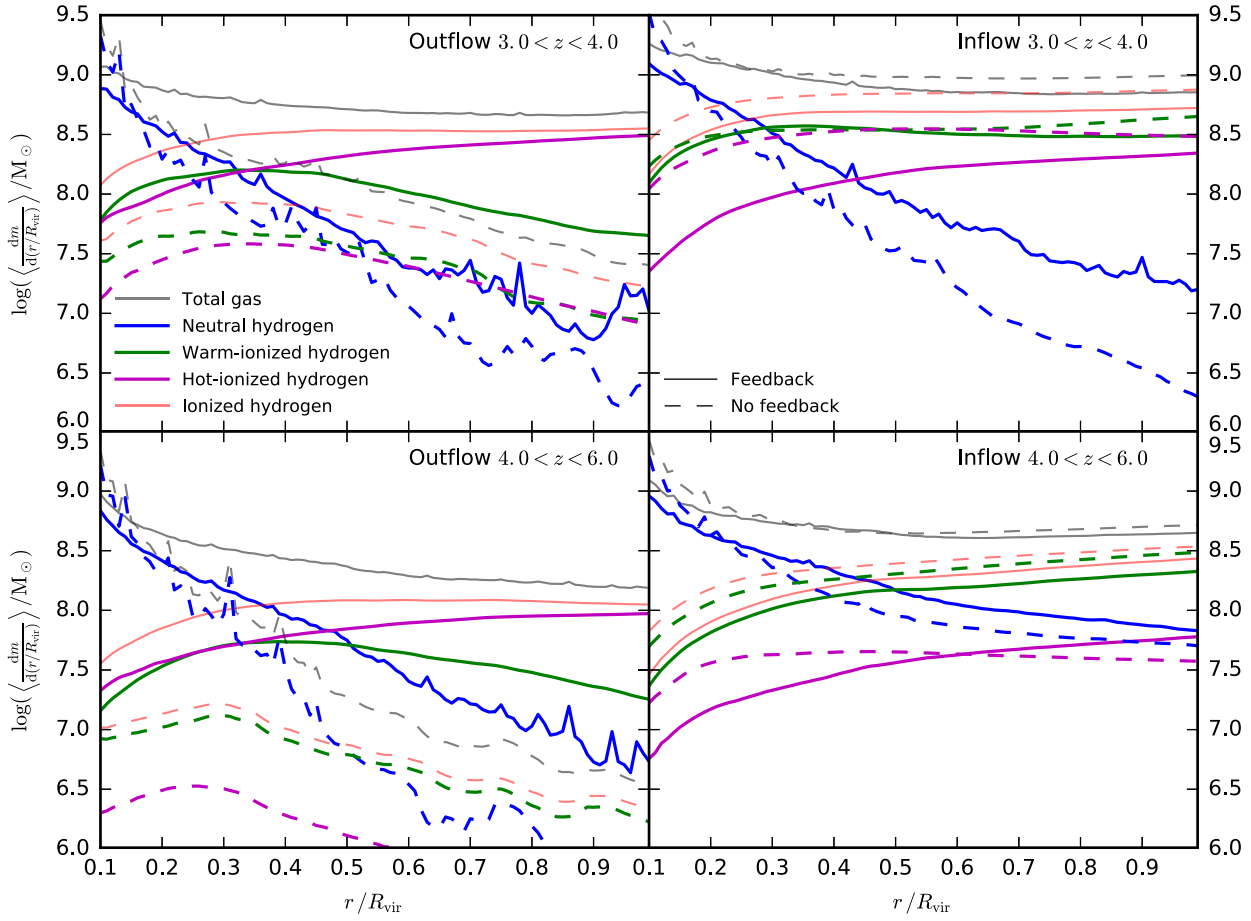

Figure 16. The effect of supernova feedback on mean stacked, spherically averaged radial mass profiles in the CGM. Solid lines correspond to simulations that include feedback and dashed lines correspond to simulations that do not include feedback (note the formatting change from Fig. 12). The left-hand/right-hand panels show profiles for gas that is radially outflowing/inflowing, respectively. Different line colours correspond to different combinations of warm-ionized, hot-ionized and neutral hydrogen, as labelled. Black lines show the total gas profile (including helium). The top/bottom panels correspond to different redshift intervals, as labelled. As in Fig. 12, the haloes included in the stack have $10.5 < \log(M_{\rm H}(z=3)/{\rm M}_\odot) < 11.2$.

distributed along filamentary structures, containing the majority of the neutral hydrogen mass. Outflowing material, while subdominant in mass, has a tendency to be aligned perpendicular to the direction of inflow and can act to fill the projected surface with neutral hydrogen, potentially forming an important contributor to the scattered Ly α signal. The effect of feedback is less pronounced on the neutral outflow for $z = 3$–4. This emphasizes the importance of satellites (and their associated tidal material) to the neutral outflowing CGM content. The high-mass resolution of our simulations makes them ideal for capturing this effect. At higher redshifts ($z = 4$–6, also observed by Wisotzki et al. 2016), the effect of feedback on the neutral, outflowing CGM content becomes more significant, indicating that Ly α emission may offer greater constraining power on subgrid feedback modelling at these redshifts.

Also of interest for Ly α emission is the velocity structure of the neutral inflowing/outflowing CGM. Our simulations predict only modest radial velocities (50–100 kms^{-1}) for both inflowing and outflowing neutral phases. Within half the halo virial radius, a larger fraction of the kinetic energy of neutral gas is in tangential motion. In particular, the outflowing neutral CGM never resembles a coherent radial outflow. This picture is somewhat in tension with the properties of the Ly α line measured around LAEs, which tends to be redshifted with respect to systemic (e.g. Erb et al. 2014; Song et al. 2014) and is most simply explained as the result of backscattering from neutral outflow moving at larger radial velocities than those reported here (Hashimoto et al. 2015). This may indicate that the properties of the neutral CGM predicted by our numerical simulations are not accurate. Alternatively, it is also possible that the spectral properties of observed Ly α lines are imprinted on the smaller scales of the ISM. In principle, our simulations combined with Ly α radiative transfer can capture these small-scale effects and we plan to return to this question in future work.

7.2 Numerical convergence of neutral CGM content

A key limitation of cosmological simulations is that the spatial resolution rapidly degrades away from the high-density ISM at the centres of haloes. In the CGM, this effect will act to smooth out density fluctuations in the gas (Fumagalli et al. 2014). This can impact the neutral CGM content in a number of ways. Low-density gas will be artificially enhanced in density (by mixing with higher density gas), enabling enhanced radiative cooling, spuriously

increasing the neutral fraction. Conversely, moderate density gas which is self-shielded against the UV background but not dense enough to self-gravitate (and thus trigger refinement, preserving the resolution) will be artificially mixed with lower density ambient gas. These two effects may balance to produce the same net neutral CGM mass but will none the less smooth out the spatial structure, with obvious implications for Ly α radiative transfer. In AMR codes, non-Lagrangian refinement criteria can be employed to explore the impact of these effects. For example, the refinement strategy of Rosdahl & Blaizot (2012), where refinement is triggered proportional to the spatial gradient of the ionization fraction will act to prevent artificial mixing of low-/moderate-density gas, alleviating this effect. We leave the application of such a refinement scheme to the simulations presented here to future work.

7.3 Missing physics

For the more massive simulated haloes in our simulated sample, the stellar masses appear to be on average too high compared to extrapolations of observational constraints (see Fig. 3). This indicates that either the efficiency of star formation or the efficiency of feedback is overestimated/underestimated, respectively.[15] Also shown in Fig. 3 is the reference EAGLE simulation, for which the predicted masses agree very well with observational constraints at low redshift (Schaye et al. 2015), and for $z = 3$, 4 at higher masses (where observational constraints are available; Furlong et al. 2015). This agreement is achieved in EAGLE by rigidly controlling the radiative losses: gas is only heated by SN if the temperature difference is $\Delta T = 10^{7.5}$ K, heating gas well above the peak of the cooling curve (Schaye et al. 2015). In our simulations (which have $\sim 10^3$ higher mass resolution and allow a cold phase to form), such an approach is not satisfactory given the ability to resolve distinct phases of SNe explosions (energy conserving versus momentum conserving; Kimm et al. 2015). None the less, it has been demonstrated in idealized simulations of galaxy disks (at a similar resolution to cosmological simulations presented here) that the delayed-thermal feedback scheme used in EAGLE gives similar results to the mechanical feedback scheme used here (when both feedback schemes are used in RAMSES at similar resolution and with the same star formation and cooling models; Rosdahl et al. 2017).

Zoom simulations have also had success in reproducing the stellar masses inferred from observations (e.g. Hopkins et al. 2014; Agertz & Kravtsov 2015; Wang et al. 2015). Wang et al. (2015) achieve this by artificially limiting radiative losses, and by utilizing very efficient radiative energy ejection into the ISM from massive stars. Agertz & Kravtsov (2015) show that they can reproduce observational constraints by combining energy and momentum injection from massive stars and supernova with a higher local star formation efficiency (they do not artificially prevent radiative losses). Hopkins et al. (2014) present a similar argument, emphasizing the importance of coupling between stellar winds, radiation pressure (including efficient trapping of infrared photons) and SN explosions for regulating star formation and generating powerful mass outflows. Muratov et al. (2015) analyse the same simulations and report mass-loading factors which are comparable to the lower mass haloes in our sample and are on average a factor $\approx$4 higher than the more massive haloes in our sample (see also Anglés-Alcázar et al. 2017; Keller et al. 2016). Increasing the outflow rates to such levels in our simulations for the more massive haloes would likely help to achieve agreement with observational constraints on stellar masses. We also note that the efficient feedback implemented in these simulations leads to a significant enhancement of neutral CGM content with respect to older simulations (Faucher-Giguère et al. 2015).

A common feature of the Hopkins et al. (2014), Wang et al. (2015) and Agertz & Kravtsov (2015) simulations is that they all employ efficient early feedback, which can pre-process the ISM before supernovae explode (indeed the important role of these mechanisms in changing the impact of SN explosions has been explored in detail by the ISM research community, e.g. Geen et al. 2015; Fierlinger et al. 2016; Wareing, Pittard & Falle 2017). As such, the absence of these feedback mechanisms in our simulations could very plausibly explain our high predicted stellar masses, despite the fact that we inject more SNe energy per unit stars formed than in these simulations. It remains to be seen however if results from such cosmological simulations can be reproduced with full, coupled radiation hydrodynamics (particularly the high assumed efficiency of radiative feedback; see Rosdahl et al. 2015; Peters et al. 2017).

Aside from radiation pressure and photoheating from local sources, there are other feedback mechanisms which are entirely absent from our simulations at present. The inclusion of stellar winds has been argued by some authors as a crucial mechanism to regulate star formation in very high resolution simulations (e.g. Gatto et al. 2017; Peters et al. 2017). Also, the importance of cosmic rays for shaping the ISM and driving outflows has been explored by various authors recently (e.g. Booth et al. 2013; Salem & Bryan 2014; Girichidis et al. 2016; Pakmor et al. 2016; Simpson et al. 2016).

8 SUMMARY

We have presented a sample of 11 cosmological zoom simulations, run down to $z = 3$, specifically designed to complement CGM observations around faint, high-redshift galaxies. We show that observations from Wisotzki et al. (2016) allow the neutral CGM to be probed in Ly α emission out to close to the virial radii of individual $z = 3$–6, $M_{\rm H} \sim 10^{11}$ M$_\odot$ haloes. Haloes in this mass and redshift range can be simulated at reasonable computational cost at high-mass and spatial resolution, opening a new window for constraining the physics of gas flows around high-redshift galaxies.

To act as a baseline for future simulations, we present here simulations including Type II SN as the sole source of feedback. This leads to stellar masses which are larger at given halo mass than is implied by extrapolation of observational constrains. Galaxy sizes and star formation rates are not in obvious tension with observations (again involving some extrapolation). Put together, the low mass of our haloes precludes forming robust conclusions when comparing to current observations.

The simulations presented here are allowed to form a cold ISM phase, a crucial step for computing realistic Ly α radiative transfer through the ISM. We also use subgrid models for star formation and SN feedback which are designed to operate at the high resolution used here, where the ISM is resolved well below kpc scales. In this paper, we lay the groundwork for interpreting future work on Ly α radiative transfer using these simulations, exploring the neutral CGM content of high-redshift haloes. Our main results are summarized as follows:

(i) Supernova feedback acts to reduce the integrated baryon content of simulated haloes by 40–85 per cent (Fig. 7 in Section 5), partly by driving outflows (with mass-loading factors ranging

[15] Despite the fact that we overinject SN energy by a factor $\approx$2–3; see Section 2.4.

between 15 and unity, Fig. 8) and partly by reducing gas inflow rates (by 20–80 per cent, Fig. 9).

(ii) The time-averaged mass in the inflowing CGM is roughly unaffected by SN feedback (Fig. 10 in Section. 5.3), but the radial velocity of inflowing warm and hot ionized gas phases is reduced by a factor 2.

(iii) Including SN feedback affects the phase distribution of inflowing hydrogen. The mass of ionized (neutral) inflowing hydrogen in the CGM is reduced (increased) by ~ 20 per cent (a factor $\sim$2, Fig. 11 in Section 5.3).

(iv) The time-averaged mass in the outflowing CGM is significantly enhanced by SN feedback, mostly in the ionized phase of hydrogen (Fig. 11 in Section 5.3), although the neutral outflowing CGM is also significantly enhanced for $z > 4$ (Fig. 16 in Section 6.3).

(v) The mass in outflowing neutral hydrogen declines strongly as outflowing gas moves away from the halo centre (Fig. 12 in Section. 6). Correspondingly, the mass in inflowing neutral hydrogen increases strongly as inflowing gas moves towards the halo centre, suggestive of a galactic fountain process.

(vi) On the other hand, the relative mass fractions of different outflowing phases of hydrogen change as a function of radius, indicating possible mass exchange between different outflowing phases. The same is true for the corresponding inflowing phases.

(vii) For $z = 3$–4, the density distribution of outflowing neutral hydrogen is broader than the density distribution of neutral inflow (Fig. 14 in Section 6.1). For $z > 4$, the density distribution of outflowing neutral hydrogen instead closely resembles the density distribution of neutral inflow, indicating an evolution of the average neutral CGM properties between $z = 3$–4 and $z = 4$–6.

(viii) Neutral outflow moves with modest radial velocities ($\sim$50 km s^{-1}, Fig. 14 in Section 6.1), with the majority of the kinetic energy instead in tangential motion with respect to the halo centre (Fig. 15 in Section 6.2).

Put together, we demonstrate that SN feedback has a significant effect on a number of properties of the neutral/ionized CGM. While these simulations are in tension with extrapolations to observationally inferred constraints on stellar masses, it remains to be seen if they can reproduce the spatially extended Ly α emission observed by MUSE, or the properties of LLS observed in high-redshift QSO spectra (we defer both comparisons to future work). Moving forwards, these observational probes of the CGM around low-mass, high-redshift galaxies will provide valuable insight for constraining more detailed cosmological simulations that include full radiation-hydrodynamics and non-equilibrium chemistry, particularly given that such simulations are only computationally feasible for this mass/redshift range at present.

ACKNOWLEDGEMENTS

We thank Matthieu Schaller for making data from the no-feedback EAGLE simulation available to us. We are grateful to the LABEX Lyon Institute of Origins (ANR-10-LABX-0066) of the Université de Lyon for its financial support within the programme 'Investissements d'Avenir' (ANR-11-IDEX-0007) of the French government operated by the National Research Agency (ANR). Simulations were run at the Common Computing Facility (CCF) of LABEX LIO. JB and JR acknowledge support for the ORAGE project from the Agence Nationale de la Recherche under grant ANR-14-CE33-0016-03. TK acknowledges support by the ERC Advanced Grant 320596 'The Emergence of Structure during the Epoch of Reionization' and the National Research Foundation of Korea to the Center for Galaxy Evolution Research (No. 2017R1A5A1070354).

REFERENCES

Agertz O., Kravtsov A. V., 2015, ApJ, 804, 18
Anglés-Alcázar D., Davé R., Özel F., Oppenheimer B. D., 2014, ApJ, 782, 84
Anglés-Alcázar D., Faucher-Giguère C.-A., Kereš D., Hopkins P. F., Quataert E., Murray N., 2017, MNRAS, 470, 4698
Aubert D., Pichon C., Colombi S., 2004, MNRAS, 352, 376
Beckmann R. S. et al., 2017, MNRAS, 472, 949
Behroozi P. S., Wechsler R. H., Conroy C., 2013, ApJ, 770, 57
Binney J., Tremaine S., 2008, Galactic Dynamics, 2nd edn. Princeton Univ. Press, Princeton, NJ
Birnboim Y., Dekel A., 2003, MNRAS, 345, 349
Booth C. M., Schaye J., 2009, MNRAS, 398, 53
Booth C. M., Agertz O., Kravtsov A. V., Gnedin N. Y., 2013, ApJ, 777, L16
Bouché N., Hohensee W., Vargas R., Kacprzak G. G., Martin C. L., Cooke J., Churchill C. W., 2012, MNRAS, 426, 801
Bouwens R. J. et al., 2016, ApJ, 833, 72
Brook C. B., Stinson G., Gibson B. K., Shen S., Macciò A. V., Obreja A., Wadsley J., Quinn T., 2014, MNRAS, 443, 3809
Brooks A. M., Governato F., Quinn T., Brook C. B., Wadsley J., 2009, ApJ, 694, 396
Bruzual G., Charlot S., 2003, MNRAS, 344, 1000
Cantalupo S., Arrigoni-Battaia F., Prochaska J. X., Hennawi J. F., Madau P., 2014, Nature, 506, 63
Ceverino D., Klypin A., 2009, ApJ, 695, 292
Chabrier G., 2003, PASP, 115, 763
Chiosi C., Bertelli G., Bressan A., 1992, ARA&A, 30, 235
Chisholm J., Tremonti C. A., Leitherer C., Chen Y., 2017, MNRAS, 469, 4831
Christensen C. R., Davé R., Governato F., Pontzen A., Brooks A., Munshi F., Quinn T., Wadsley J., 2016, ApJ, 824, 57
Cooper T. J., Simcoe R. A., Cooksey K. L., O'Meara J. M., Torrey P., 2015, ApJ, 812, 58
Crain R. A. et al., 2015, MNRAS, 450, 1937
Dijkstra M., 2014, PASA, 31, e040
Dijkstra M., Kramer R., 2012, MNRAS, 424, 1672
Dijkstra M., Loeb A., 2009, MNRAS, 400, 1109
Erb D. K. et al., 2014, ApJ, 795, 33
Fardal M. A., Katz N., Gardner J. P., Hernquist L., Weinberg D. H., Davé R., 2001, ApJ, 562, 605
Faucher-Giguère C.-A., Kereš D., Dijkstra M., Hernquist L., Zaldarriaga M., 2010, ApJ, 725, 633
Faucher-Giguère C.-A., Kereš D., Ma C.-P., 2011, MNRAS, 417, 2982
Faucher-Giguère C.-A., Hopkins P. F., Kereš D., Muratov A. L., Quataert E., Murray N., 2015, MNRAS, 449, 987
Federrath C., Klessen R. S., 2012, ApJ, 761, 156
Ferland G. J., Korista K. T., Verner D. A., Ferguson J. W., Kingdon J. B., Verner E. M., 1998, PASP, 110, 761
Fierlinger K. M., Burkert A., Ntormousi E., Fierlinger P., Schartmann M., Ballone A., Krause M. G. H., Diehl R., 2016, MNRAS, 456, 710
Fumagalli M., Hennawi J. F., Prochaska J. X., Kasen D., Dekel A., Ceverino D., Primack J., 2014, ApJ, 780, 74
Furlong M. et al., 2015, MNRAS, 450, 4486
Gatto A. et al., 2017, MNRAS, 466, 1903
Geen S., Rosdahl J., Blaizot J., Devriendt J., Slyz A., 2015, MNRAS, 448, 3248
Girichidis P. et al., 2016, ApJ, 816, L19
Gnedin N. Y., 2000, ApJ, 542, 535
Gnedin N. Y., Tassis K., Kravtsov A. V., 2009, ApJ, 697, 55
Goerdt T., Dekel A., Sternberg A., Ceverino D., Teyssier R., Primack J. R., 2010, MNRAS, 407, 613
Gronke M., Dijkstra M., 2016, ApJ, 826, 14
Haardt F., Madau P., 1996, ApJ, 461, 20

Hahn O., Abel T., 2011, MNRAS, 415, 2101
Hashimoto T. et al., 2015, ApJ, 812, 157
Heckman T. M., Thompson T. A., 2017, preprint (arXiv:1701.09062)
Hopkins P. F., Kereš D., Oñorbe J., Faucher-Giguère C.-A., Quataert E., Murray N., Bullock J. S., 2014, MNRAS, 445, 581
Hopkins P. F. et al., 2017, preprint (arXiv:1702.06148)
Hu C.-Y., Naab T., Walch S., Glover S. C. O., Clark P. C., 2016, MNRAS, 458, 3528
Iliev I. T., Mellema G., Shapiro P. R., Pen U.-L., 2007, MNRAS, 376, 534
Katz H., Kimm T., Sijacki D., Haehnelt M. G., 2017, MNRAS, 468, 4831
Keller B. W., Wadsley J., Couchman H. M. P., 2016, MNRAS, 463, 1431
Kereš D., Katz N., Fardal M., Davé R., Weinberg D. H., 2009, MNRAS, 395, 160
Kimm T., Cen R., 2014, ApJ, 788, 121
Kimm T., Cen R., Devriendt J., Dubois Y., Slyz A., 2015, MNRAS, 451, 2900
Kimm T., Katz H., Haehnelt M., Rosdahl J., Devriendt J., Slyz A., 2017, MNRAS, 466, 4826
Leclercq F. et al., 2017, A&A, 608, 8
Moster B. P., Naab T., White S. D. M., 2013, MNRAS, 428, 3121
Muratov A. L., Kereš D., Faucher-Giguère C.-A., Hopkins P. F., Quataert E., Murray N., 2015, MNRAS, 454, 2691
Nelson D., Genel S., Vogelsberger M., Springel V., Sijacki D., Torrey P., Hernquist L., 2015, MNRAS, 448, 59
Ocvirk P., Pichon C., Teyssier R., 2008, MNRAS, 390, 1326
Oñorbe J., Hennawi J. F., Lukić Z., 2017, ApJ, 837, 106
Oppenheimer B. D. et al., 2016, MNRAS, 460, 2157
Padoan P., Nordlund Å., 2011, ApJ, 730, 40
Pakmor R., Pfrommer C., Simpson C. M., Springel V., 2016, ApJ, 824, L30
Péroux C., Dessauges-Zavadsky M., D'Odorico S., Kim T.-S., McMahon R. G., 2007, MNRAS, 382, 177
Peters T. et al., 2017, MNRAS, 466, 3293
Planck Collaboration XVI, 2014, A&A, 571, A16
Powell L. C., Slyz A., Devriendt J., 2011, MNRAS, 414, 3671
Prochaska J. X., O'Meara J. M., Fumagalli M., Bernstein R. A., Burles S. M., 2015, ApJS, 221, 2
Rosdahl J., Blaizot J., 2012, MNRAS, 423, 344
Rosdahl J., Schaye J., Teyssier R., Agertz O., 2015, MNRAS, 451, 34
Rosdahl J., Schaye J., Dubois Y., Kimm T., Teyssier R., 2017, MNRAS, 466, 11
Rosen A., Bregman J. N., 1995, ApJ, 440, 634
Salem M., Bryan G. L., 2014, MNRAS, 437, 3312
Schaller M. et al., 2015, MNRAS, 451, 1247
Schaye J. et al., 2015, MNRAS, 446, 521
Schmidt M., 1959, ApJ, 129, 243
Simpson C. M., Pakmor R., Marinacci F., Pfrommer C., Springel V., Glover S. C. O., Clark P. C., Smith R. J., 2016, ApJ, 827, L29
Song M. et al., 2014, ApJ, 791, 3
Steidel C. C., Erb D. K., Shapley A. E., Pettini M., Reddy N., Bogosavljević M., Rudie G. C., Rakic O., 2010, ApJ, 717, 289
Taniguchi Y. et al., 2001, ApJ, 559, L9
Teyssier R., 2002, A&A, 385, 337
Tremmel M., Karcher M., Governato F., Volonteri M., Quinn T. R., Pontzen A., Anderson L., Bellovary J., 2017, MNRAS, 470, 1121
Tweed D., Devriendt J., Blaizot J., Colombi S., Slyz A., 2009, A&A, 506, 647
van de Voort F., Schaye J., Booth C. M., Haas M. R., Dalla Vecchia C., 2011, MNRAS, 414, 2458
van de Voort F., Schaye J., Altay G., Theuns T., 2012, MNRAS, 421, 2809
Verhamme A., Schaerer D., Atek H., Tapken C., 2008, A&A, 491, 89
Verhamme A., Dubois Y., Blaizot J., Garel T., Bacon R., Devriendt J., Guiderdoni B., Slyz A., 2012, A&A, 546, A111
Vogelsberger M., Genel S., Sijacki D., Torrey P., Springel V., Hernquist L., 2013, MNRAS, 436, 3031
Vogelsberger M. et al., 2014, MNRAS, 444, 1518
Wang L., Dutton A. A., Stinson G. S., Macciò A. V., Penzo C., Kang X., Keller B. W., Wadsley J., 2015, MNRAS, 454, 83
Wang L., Dutton A. A., Stinson G. S., Macciò A. V., Gutcke T., Kang X., 2017, MNRAS, 466, 4858
Wareing C. J., Pittard J. M., Falle S. A. E. G., 2017, MNRAS, 470, 2283
Wise J. H., Demchenko V. G., Halicek M. T., Norman M. L., Turk M. J., Abel T., Smith B. D., 2014, MNRAS, 442, 2560
Wisotzki L. et al., 2016, A&A, 587, A98

APPENDIX A: RADIAL MASS PROFILES: MASS AND REDSHIFT TRENDS

To explore how the results presented in Fig. 12 depend on redshift and halo mass, we present radial mass profiles for two stacking intervals in redshift and two intervals in halo mass in Fig. A1. While the radial gradients of each phase are qualitatively similar for each of the stacks considered, the relative contributions in mass from each phase do vary significantly from stack to stack.

Focusing on neutral CGM content, in general, the relative importance of the neutral CGM increases with redshift. In the lower halo mass interval, the relative contribution from both neutral inflow and outflow are significantly enhanced in the higher redshift interval. For the higher halo mass interval, the relative contribution of neutral inflow is significantly enhanced in the higher redshift interval but neutral outflowing mass remains comparable with redshift.

For the ionized phases, the relative contribution of hot-ionized inflow drops significantly at higher redshifts while warm-ionized hydrogen is always the dominant inflowing phase (by mass) away from the central galaxy ($r > 0.4R_{\rm vir}$). For outflowing ionized phases, the hot phase always dominates for the more massive halo stack. For the lower mass stack, the warm-ionized phase is comparable to the hot-ionized phase, and forms the largest contributor to outflowing mass at all radii in the $4 < z < 6$ stack.

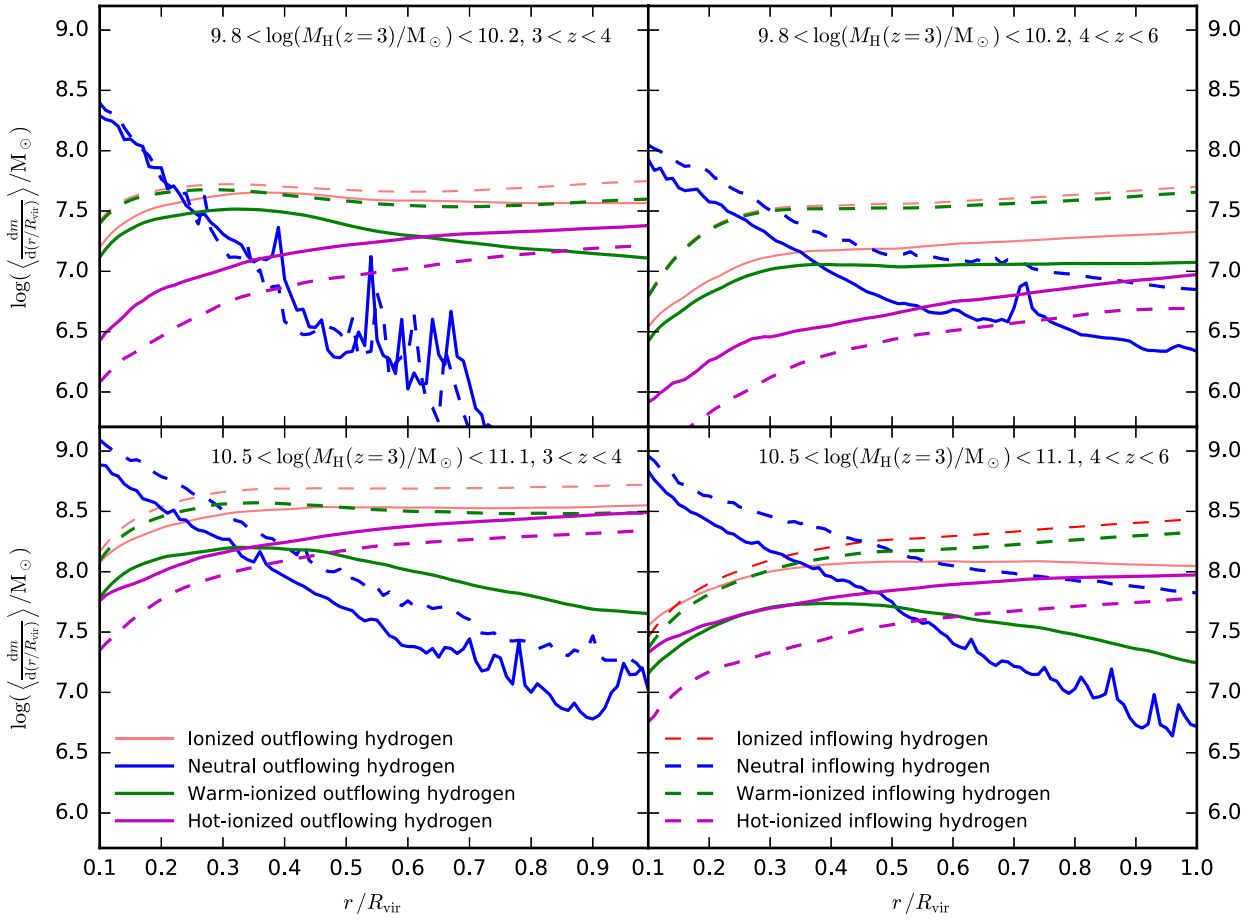

Figure A1. Mass and redshift trends for different phases of circumgalactic hydrogen. Spherically integrated radial mass profiles are plotted as a function of radius. The profiles are split between different combinations of inflowing/outflowing and warm-ionized/hot-ionized/neutral phases of hydrogen. Formatting follows Fig. 12. Each panel corresponds to a different combination of stacking intervals in halo mass and redshift, as labelled.

This paper has been typeset from a TEX/LATEX file prepared by the author.